SURFACE ROUGHNESS ARISING FROM ULTRAFAST LASER TECHNIQUES PERFORMED ON GLASS FOR FABRICATING X-RAY OPTICS

by

Winona C. Esher

A Thesis Submitted to the Faculty of the

JAMES C. WYANT COLLEGE OF OPTICAL SCIENCES

In Partial Fulfillment of the Requirements

For the Degree of

MASTER OF SCIENCE

In the Graduate College

THE UNIVERSITY OF ARIZONA

2025

THE UNIVERSITY OF ARIZONA
GRADUATE COLLEGE

As members of the Master's Committee, we certify that we have read the thesis prepared by **Winona Catalina Esher**, titled ***Surface Roughness Arising from Ultrafast Laser Techniques Performed on Glass for Fabricating X-Ray Optics,*** and recommend that it be accepted as fulfilling the thesis requirement for the Master's Degree.

Professor Brandon D. Chalifoux Date: 4/23/25

Professor José M. Sasián Date: 4/23/25

Professor Daewook Kim Date: 4/23/25

Final approval and acceptance of this thesis is contingent upon the candidate's submission of the final copies of the thesis to the Graduate College.

I hereby certify that I have read this thesis prepared under my direction and recommend that it be accepted as fulfilling the Master's requirement.

Professor Brandon D. Chalifoux
Master's Thesis Committee Chair
Wyant College of Optical Sciences Date: 4/23/25

Acknowledgements

I would first like to thank Dr. Brandon Chalifoux for his invaluable guidance and consistent feedback throughout my graduate career and my time in the Lightweight Optics Lab. I am deeply grateful for the opportunity to work on challenging projects and broaden my understanding of x-ray telescope systems.

The members of the lab deserve a big thank you for listening to my research anomalies and helping me with any and all lab problems I encountered. Especially to those who sat next to me every day, Carolyn Hokin, Kevin Laverty, Lakshmi Gurunathan, and Kyle Ettinger. One thing I will never forget working in the lab with this research group is to always multiply your research timeline by pi, it has held true every time without fail. Lastly, nothing would have been possible without financial support for this research provided by National Aeronautics and Space Administration (NASA), Science Mission Directorate (SMD), grant 80NSSC22K1484.

I would also like to thank my friends and peers that I am so glad I've met throughout both my undergraduate and graduate career at the James C. Wyant College of Optical Sciences. Not only were the many late nights of studying not possible without them, but my academic career significantly improved with their support.

One last thank you to my parents for their continual encouragement throughout my academic career, I truly could not have done it without their support.

All Park Systems NX20 AFM images and data were collected in the W.M. Keck Center for Nano-Scale Imaging, RRID:SCR_022884, in the Department of Chemistry and Biochemistry at the University of Arizona. This instrument purchase was partially supported by Arizona Technology and Research Initiative Fund (A.R.S.§15-1648).

Table of Contents

List of Figures......5
Abstract......8
Chapter 1 – Introduction......9
1.1 X-ray telescopes......9
1.1.1 X-ray optics fabrication......10
1.1.2 Surface roughness requirements for x-ray optics......12
1.2 Ultrafast laser processing techniques......16
Chapter 2 – Surface Roughness of Fabrication Techniques......20
2.1 Motivation......20
2.2 Methods......21
2.2.1 Experimental Plan......21
2.2.2 Atomic force microscope (AFM)......26
2.2.3 White-light interferometer (WLI)......29
2.3 Results......31
2.3.1 Surface quality and power spectral density (PSD)......31
2.4 Discussion......39
Chapter 3 – Laser-Induced Surface Nanopillars......42
3.1 Motivation......42
3.2 Parametric study......45
3.3 Surface structure characterization......57
3.4 Discussion......63
Chapter 4 – Conclusion......64
References......66

List of Figures

Figure 1. X-ray optics telescope cutaway example. Note two reflections – Primary (often parabolas) and secondary (often hyperbolas). Similar to a Gregorian telescope but with grazing incidence. Two reflections means reflectance is even more important. 10

Figure 2. Areal mass vs angular resolution for various x-ray telescope missions [1]. 11

Figure 3. The four major steps to build a mirror assembly for the Lynx observatory. a) Fabrication of mirror segments, each measuring about 100 mm x 100 mm x 0.5 mm. b) Mirror segments are combined into mirror modules. c) Mirror modules are combined into metashells. d) Metashells are combined into a mirror assembly [3]. 12

Figure 4. Comparison of different surface roughness' of ULE and the resulting reflectivity of both mirror surfaces at grazing angles of incidence for 0, 0.5, and 10 nm rms surface roughness at 6 keV [4]. Notice how quickly the reflectivity drops with increasing surface roughness, 10 nm is relatively large and reduces mirror reflectivity significantly. The critical angle for ULE here is 0.351°. 14

Figure 5. Simulated table showing mirror reflectivity of ULE (both mirror surfaces) at grazing angle of incidence for 0, 1, and 5 nm rms surface roughness at 1 keV [4]. 15

Figure 6. Simulated table showing mirror reflectivity of ULE at 1° grazing angle of incidence for 0, 1, and 5 nm rms surface roughness [4]. 15

Figure 7. Heatmaps showing etching selectivity of laser irradiated material etched in an 8 mol/L KOH solution at 85 C. a) Selectivity of 1D channels – each triplet row (from bottom to top) corresponds to writing depths of 250, 500, and 750 μm in fused silica. b) Selectivity of 2D planar surfaces – each pair of rows correspond to etchant penetration into near (bottom) and far (top) surfaces of the substrate. c) Selectivity obtained for 2D planar surfaces as a function of scan separations. Pulse energy and repetition rate were kept constant at 200 nJ and 250 kHz respectively [7]. 17

Figure 8. Illustration of slumping process: A thin glass sheet is placed on top of a cylindrical mandrel in an oven. As the temperature increases to about 600 °C, the glass softens and conforms to the shape of the mandrel [9]. 18

Figure 9. Biomimetic surface structures and refractive index gradient images. a) Moth eyes. b) scanning electron microscope (SEM) image of ommatidia (individual units of the eye). c) flat substrate. d) 1D grating surface. e) multilevel surface profile. f) continuous conical surface profile. g) continuous parabolic conical surface profile [11]. 19

Figure 10. a-d) Photograph of a cicada wing with respective SEM images at different magnifications. e-h) Photogrpah of a fused silica plate and SEM images of the lasered spot. [10] 20

Figure 11. Process flow diagram of Iteration 1 samples. 23

Figure 12. Process flow diagram of Iteration 2 samples. 24

Figure 13. a) Samples created and used for the first iteration of the experiment. b) Samples created and used for the second iteration of the experiment, note the flexures moved up to make measuring easier. 1 μm x 1 μm area was used for AFM measurements. WLI measurements used 0.17 mm x 0.17 mm in approximately the same locations. 25

Figure 14. Basic AFM depiction 27

Figure 15. a) Raw AFM image file of unprocessed ULE surface from iteration 1. b) Processed AFM image file of unprocessed ULE surface from iteration 1. c) Statistical Quantities in Gwyddion used to identify rms surface roughness. 28

Figure 16. Optical schematic of WLI microscope [16]. 30

Figure 17. Example of a composite power spectral density of an optical surface across different spatial scale lengths using different measurement techniques [19]. 32

Figure 18. Power spectral density of pre-processed samples of iteration 2 (1 mm thick ULE) for WLI and AFM measurements. 34

Figure 19. Power spectral density of post-processed samples of iteration 2 (1 mm thick ULE) for WLI and AFM measurements. 34

Figure 20. Surface roughness measurements using the WLI on iteration 1 samples (0.375 mm thick ULE). Four 0.17 mm x 0.17 mm fields were measured on each of 2 etched samples, 2 slumped samples and 2 control samples. 36

Figure 21. Surface roughness measurements using the AFM for iteration 1 samples (0.375 mm thick ULE). Four 1 μm x 1 μm fields were measured on each of 2 etched samples, 2 slumped samples and 2 control samples. (Note only measurements after processing were recorded) 37

Figure 22. Surface roughness measurements using the WLI for iteration 2 samples (1 mm thick ULE). Four 0.17 mm x 0.17 mm fields were measured on four etched samples and four control samples. The small data points detached from the box plots are outliers in the data set. 38

Figure 23. Surface roughness measurements using the AFM for iteration 2 samples (1 mm thick ULE). Four 1 μm x 1 μm fields were measured on four etched samples and four control samples. 39

Figure 24. AFM images of control samples. Left: Iteration 1 measuring 0.577 nm rms. Right: Iteration 2 measuring 0.368 nm rms. Note the height is different for each iteration. Notice the similarity of the unprocessed ULE surface – both show polishing effects and some scratches. 40

Figure 25. AFM images of etched samples. Left: Iteration 1 measuring 0.676 nm rms. Right: Iteration 2 measuring 0.259 nm rms. Note the height is different for each iteration. Notice the similarity of a 'fuzzy' image – both show some darker regions and some lighter regions. 40

Figure 26. AFM image of slumped sample. Iteration 1 measuring 0.667 nm rms. Notice the stark difference between this slumping result compared to the unprocessed samples. 41

Figure 27. Depiction of desired reflections (mirror surface) and undesired reflections (back surface) of a cut view of an x-ray telescope. 42

Figure 28. Diagram of metrology configuration where an interferometer is measuring the front surface of the x-ray mirror through the back surface. 43

Figure 29. Depictions of incident light propagation through (a) single layer thin-film (n_s>n), (b) micro-scale array of structures, (c) nano-scale array of structures [20]. 44

Figure 30. The first parameter scan performed on fused silica. Pulse energy was stepped from 1 μJ to 2 μJ from right to left in 0.01 μJ steps spanning 20 mm in the center of the sample. *Not to scale. 47

Figure 31. 40x DIC microscope images of ablation threshold found from first parameter scan. Left: E_p = 1.51 μJ, (fluence = 6.16 $Jcm2$) ablation seen in the 4th line from the bottom. Right: E_p = 1.5 μJ, (fluence = 6.12 $Jcm2$) ablation free lines. 48

Figure 32. Depiction of first parameter grid scan on fused silica sample with varying E_p from 1.2 μJ to 1.4 μJ, and varying scan range from 1 to 7 scans. *Not to scale. 49

Figure 33. 10x DIC microscope image of grid scan 1. Column corresponding to E_p from right to left [μJ]: 1.19, 1.23, 1.26, 1.33, 1.37 50

Figure 34. 10x DIC microscope image of grid scan 2. Column corresponding to E_p from right to left [μJ]: 1.0, 1.04, 1.08, 1.12, 1.2. The red square indicates a region of interest for the following parameter test. 51

Figure 35. 10x DIC microscope image of rows 4 – 6 of the rectangular modifications on fused silica. 53

Figure 36. Microscope DIC images of 2 mm square modification. Left: 4x objective showing surface figure error. Right: 40x objective of top left region showing surface figure error created ablation. 54

Figure 37. Microscope DIC images of second 2 mm square. Left: 4x objective showing slight surface figure error. Right: 40x objective of bottom right region with little to no surface defects. 54

Figure 38. 4x microscope DIC image of the right side of row 3 & 4 of the first ULE parameter scan. 55

Figure 39. DIC microscope images of the right side of the second parameter scan on ULE. A) 20x objective showing rows 3 & 4. B) 40x objective showing row 3. 56

Figure 40. 10x microscope DIC image of fused silica grid scan 2. (rows 5-6, columns 3-4). 58

Figure 41. 1 μm x 1 μm AFM images corresponding to the square modifications of interest on fused silica grid scan 2 (see previous figure for correlation). The peak-to-valley heights are noted on each image. 59

Figure 42. 40x microscope DIC image of the left side of row 3 of the second parameter scan on ULE. This was 4 scans at Ep = 1 μJ. 60

Figure 43. Two 1 μm x 1 μm AFM fields measured on row 3 of the second ULE parameter scan. Left: measured in the middle of the sample. Right: measured on the right side of the sample. Laser parameters:4 scans at Ep = 1 μJ, f = 25 kHz, Δ = 3 μm, d = 1.25 μm, τp = 350 fs. 60

Figure 44. Interferometric image of the 1-inch fused silica wafer using a HeNe source. The highlighted red square is the second 2 mm square demonstrating lower reflectance. 62

Figure 45. Interferometric images of the 1-inch ULE wafer with a HeNe source. Left: Full wafer image with red rectangle highlighting the second parameter scan of 2 mm long rectangular modifications. Right: The third row of the rectangular modifications highlighted by the red outline. 63

Abstract

X-ray astronomy uses grazing incidence optics that require sub-nanometer surface roughness and nanometer-level surface figure accuracy before and after fabrication. To maintain these precise surface characteristics, flexures can be incorporated into the mirror geometry, allowing controlled deformation of the reflecting region. Achieving the complex geometry of flexures on glass substrates is done with ultrafast laser assisted chemical etching. This thesis tests how chemical etching affects the surface roughness of glass mirror substrates (fused silica and Corning ULE) in hopes that chemical etching does not degrade the surface further than the initial surface roughness. It was determined that chemical etching did not significantly degrade the surface roughness of the glass substrate. The structure of an x-ray telescope system requires high reflectance on the mirror side, while having low reflectance on the back surface. To measure the mirror surface through the back surface, an anti-reflection (AR) coating can be helpful to provide low reflectance on the back surface. Laser-induced modifications on the surface of a transparent substrate, dubbed nanopillars, are a potential solution to create a long-term stable AR coating. Due to nanopillars on the substrate surface being hundreds of nanometers tall, they could be a viable solution to provide low reflectance for the x-ray band and visible light. This thesis evaluates the formation of nanopillars on fused silica and ULE glass to find optimal parameters for creating an AR coating. Using low pulse energy and multiple passes over the same laser-modified area achieved the desired nanopillar structures about 300 nm tall.

Chapter 1 – Introduction

1.1 X-ray telescopes

An x-ray telescope comprises thin curved stacked mirror shells that efficiently reflect x-ray wavelengths, typically on the scale of 1 nm wavelength or less, depending on the energy (in keV) used [1]. An example of x-ray telescope geometry is seen in Figure 1. Typical x-ray energy used for performance specification is 1 keV which is equivalent to 1.2 nm wavelength. X-ray optics operate using grazing incidence light to focus on a small detection area of a high-performance detector. While CCD's were initially used in x-ray systems, but CMOS direct imagers are now preferred in some applications due to their faster readout rates and higher spatial resolution [1]. Grazing incidence angle in combination of a smooth reflecting region is necessary for high reflectance over a wide range of wavelengths. The projected area of each mirror is small, so nesting of the curved mirrors is required, making thin mirrors more beneficial. Nested, thin x-ray telescope mirrors allow many mirrors to capture light at the grazing angle, which contrasts typical telescope mirrors for longer wavelengths that use closer to normal incidence light. X-ray telescope designs using multiple mirror stacks allow for a larger combined collecting area which therefore achieves better imaging or more photons, depending on the function, either telescope or observatory [2].

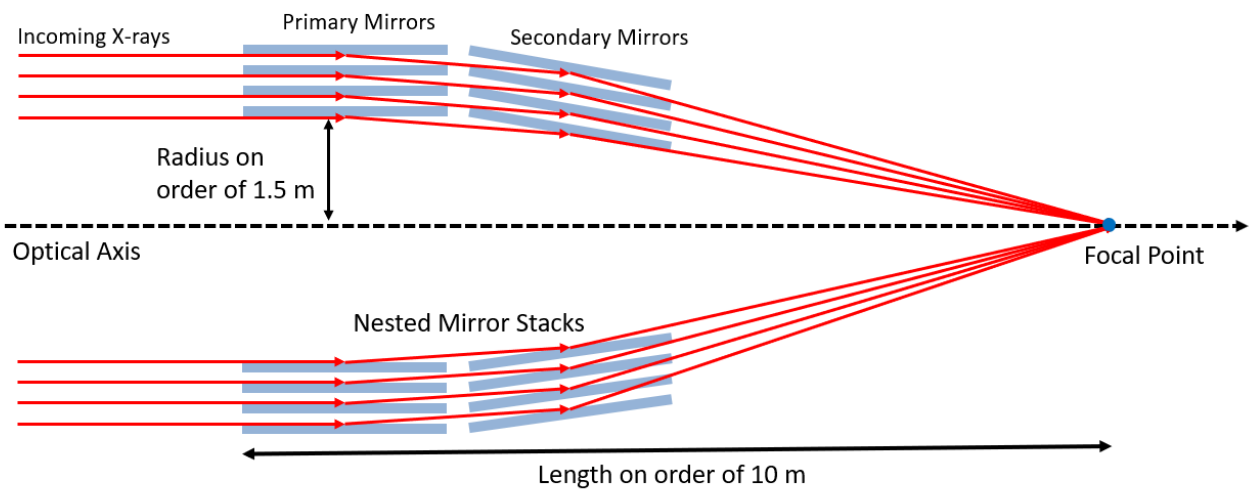

Figure 1. X-ray optics telescope cutaway example. Note two reflections – Primary (often parabolas) and secondary (often hyperbolas). Similar to a Gregorian telescope but with grazing incidence. Two reflections means reflectance is even more important.

1.1.1 X-ray optics fabrication

Over the last several decades, x-ray telescope systems focus on balancing the goals of using lightweight, easy-to-manufacture optics and achieving high angular resolution [1]. Metal mirrors have been the typical choice for many x-ray telescope missions due to fabrication techniques that enable them to be thin and lightweight but tend to sacrifice high angular resolution (sometimes referred to as half-power diameter [HPD]). On the other hand, very thick and stable substrates have been used due to their high angular resolution capabilities and ability to not result in any mount-induced deformations. Chandra, an x-ray telescope launched in 1999, has incredible angular resolution (0.5 arcsec HPD), but paired with four 16-24 mm thick mirrors of Zerodur [1]. The comparison of angular resolution and mass to effective areas of past x-ray telescope missions is shown in Figure 2. For missions of the past, there has always been a tradeoff of either angular resolution or lightweight manufacturability.

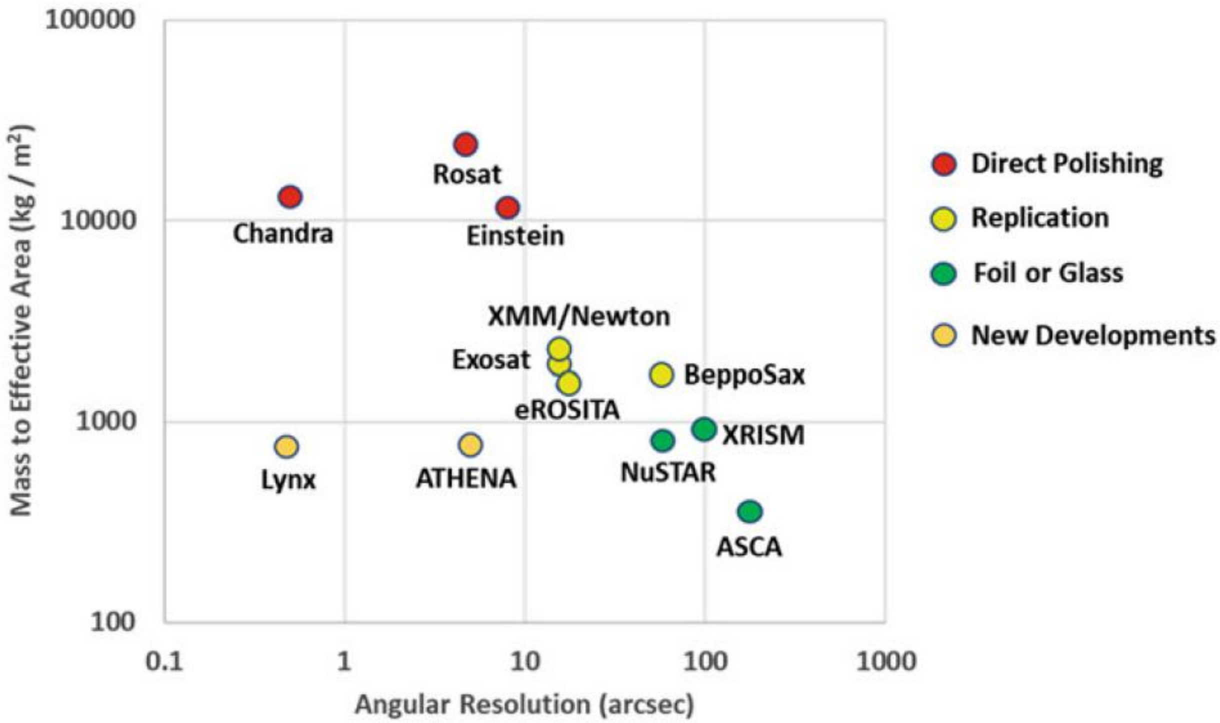

Figure 2. Areal mass vs angular resolution for various x-ray telescope missions [1].

The fabrication of the mirror shells may go through several different processes that have the possibility to negatively affect the surface roughness. Direct fabrication of the mirror shells is done by the typical grind and polish technique which allows the surface figure of the optic to be polished to 0.5 nm or less [1]. The optic can then be coated with a highly reflective metal such as gold or iridium. Replication is another fabrication technique that takes the figure of one completed mirror module and aims to replicate the figure on subsequent others. This method does not exactly match the initial mirror in terms of resolution, and has demonstrated worse performance compared to direct fabrication [1]. One replication technique is slumping, where glass can be slumped into the desired shape for the reflectors and maintain the smooth surface. Segmented optics of the mirror shell for both primary and secondary parts were found to be a solution for low cost because smaller segments could be used to replicate the reflectors of the large full shell mirrors. One recent example of the thin mirror stacks has been demonstrated for the Lynx observatory, shown in Figure 3 below [3]. These types of segmented optics could also be fabricated out of glass rather than silicon to decrease mass and increase stability of surface roughness [1].

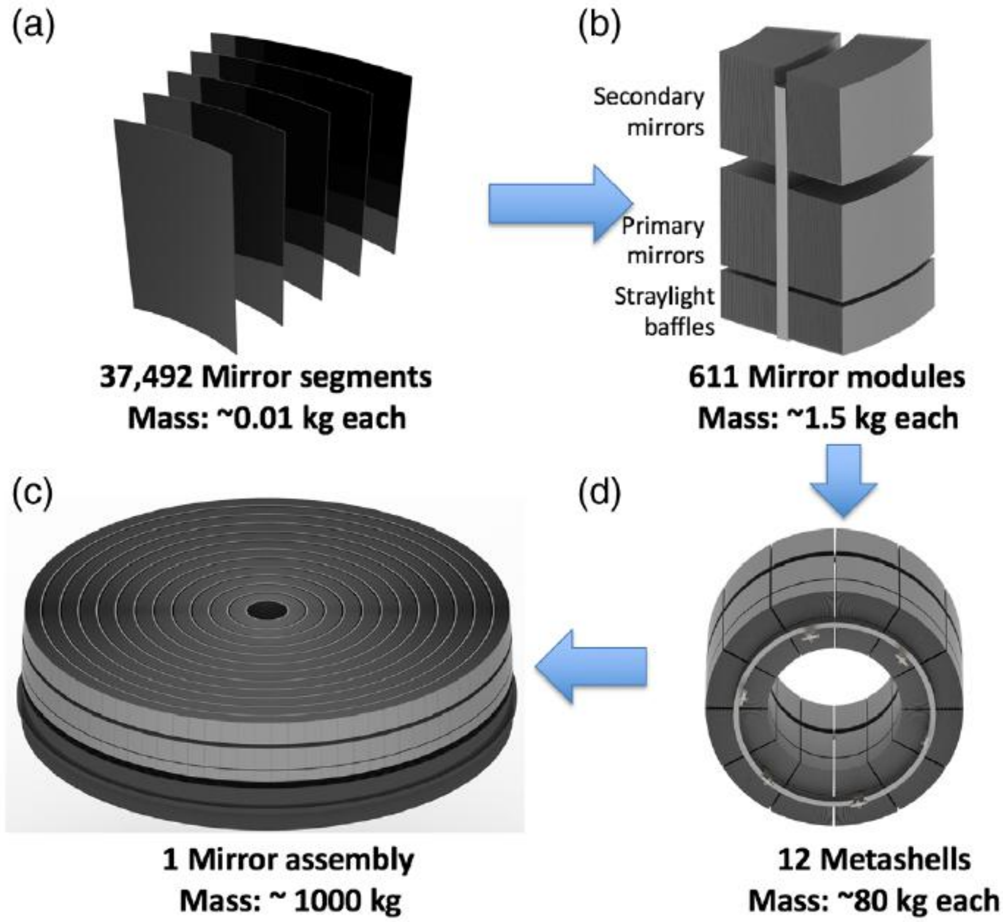

Figure 3. The four major steps to build a mirror assembly for the Lynx observatory. a) Fabrication of mirror segments, each measuring about 100 mm x 100 mm x 0.5 mm. b) Mirror segments are combined into mirror modules. c) Mirror modules are combined into metashells. d) Metashells are combined into a mirror assembly [3].

1.1.2 Surface roughness requirements for x-ray optics

The experimental goal of the testing fabrication techniques of etching and slumping on two different ULE substrates should not induce any roughness causing the measured surface roughness to exceed 0.5 nm. For x-ray optics, the performance of the grazing incidence of light is highly dependent on the surface quality of the optical surface. Due to the nature of x-ray optics relying on short wavelength, this means that the surface of the stacked mirror shells must have low surface roughness to operate at grazing incidence. Maintaining a smooth surface reduces any irregularities on the surface that may lead to unwanted scattering of light. Low-frequency and high-frequency irregularities both negatively affect the overall figure accuracy and surface roughness. In order for x-rays to have efficient specular reflection, the surface roughness of the optic must be on the same scale as the incident wavelength [1]. Typically, the required surface roughness for one of these x-ray mirror substrates is less than 0.5 nm rms to limit any scattering. Scattering is inevitable, but the amount of flux scattered,

$$\frac{I_s}{I_o} = 1 - e^{-\left(\frac{4\pi\ \sigma\ sin\alpha}{\lambda}\right)^2} \tag{1}$$

can be controlled with low surface roughness when the grazing incidence angle is small, where I_s is the scattered x-ray intensity, I_o is the incident x-ray intensity, σ is rms surface roughness, α is the grazing angle, and λ is the x-ray wavelength [1].

When the segmented mirrors are made of glass, the surface roughness available is sub-0.5 nm, ideal for x-ray optics. When coatings are applied to substrates, the deposition of thin films often degrade roughness, so maintaining less than 0.5 nm rms is important. Below is an example of the reflectivity of ULE at a surface roughness of 0.5 nm compared to a perfectly smooth surface (0 nm) and a much rougher surface (10 nm). The Center for X-Ray Optics research group within Lawrence Berkeley National Laboratory has a useful X-Ray Interactions with Matter tool that can simulate the x-ray reflectivity of a mirror given a material, rms roughness value, energy and angle [4]. X-ray optics operate leveraging total external reflection, which occurs when the incident angle is below the critical angle, preventing the light ray from transmitting into the second medium [5]. When the incident light contacts the substrate at an angle less than the critical angle, the light is reflected. The critical angle for x-ray optics is often 0.1° – 0.5°, so grazing angles of incidence are required.

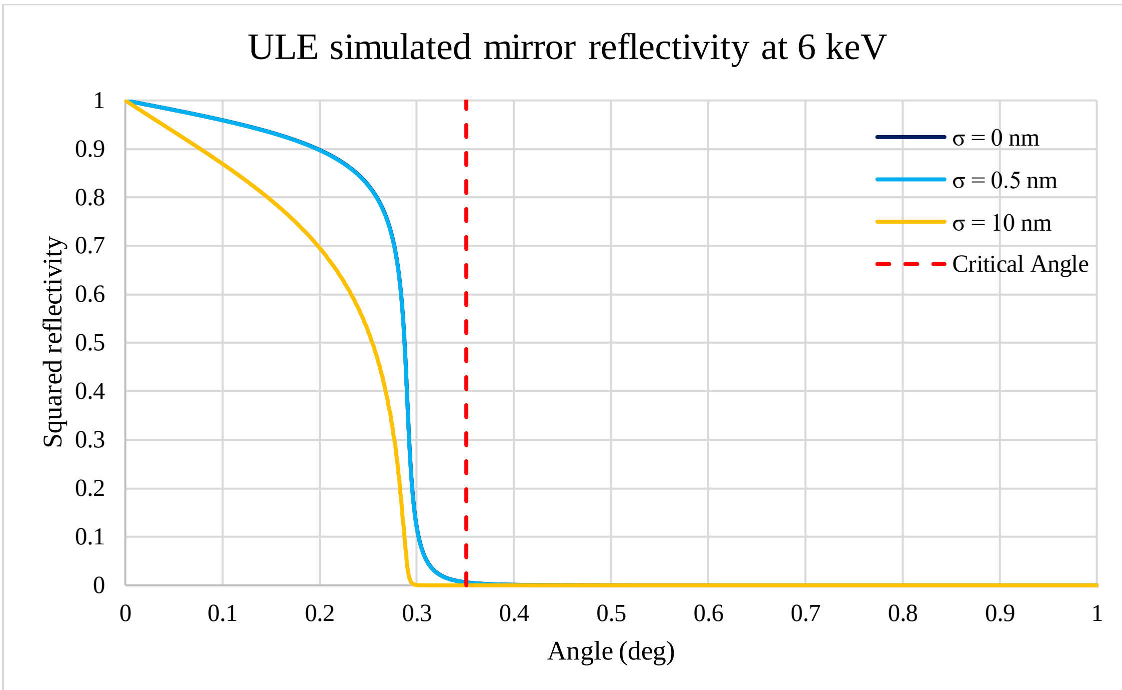

Figure 4. Comparison of different surface roughness' of ULE and the resulting reflectivity of both mirror surfaces at grazing angles of incidence for 0, 0.5, and 10 nm rms surface roughness at 6 keV [4]. Notice how quickly the reflectivity drops with increasing surface roughness, 10 nm is relatively large and reduces mirror reflectivity significantly. The critical angle for ULE here is 0.351°.

Below are additional plots relating rms surface roughness to x-ray reflectivity performance while holding energy constant (Figure 5) and holding angle of incidence constant (Figure 6). Note the difference of the reflectivity drop off with an increase in surface roughness.

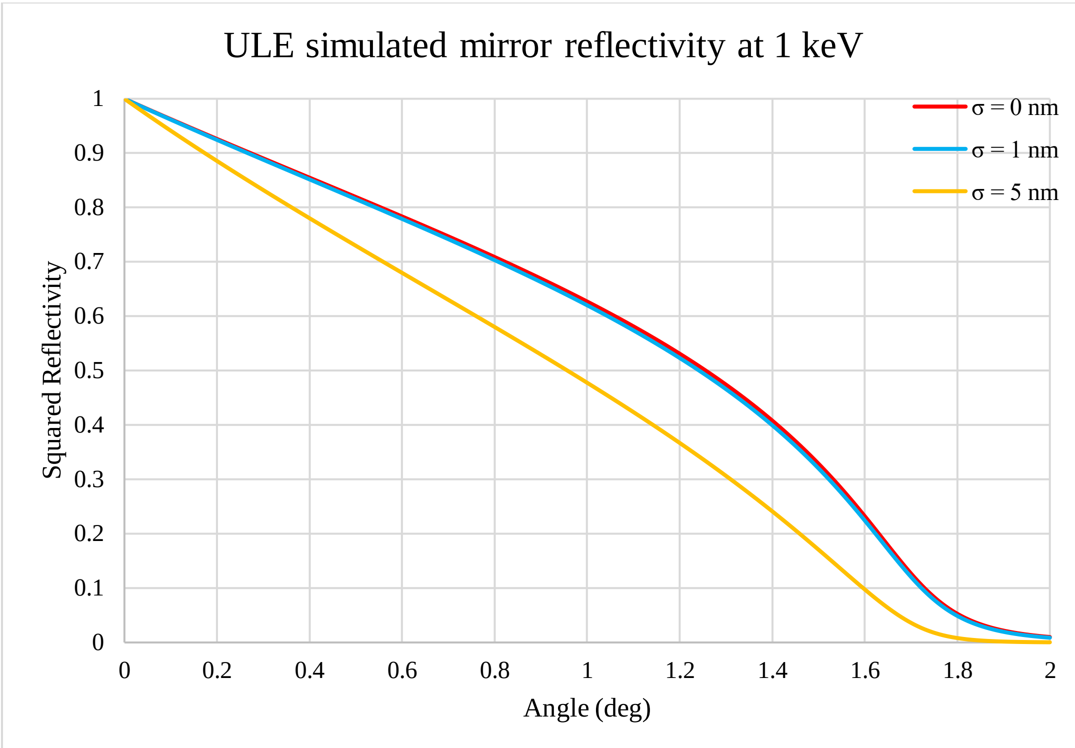

Figure 5. Simulated table showing mirror reflectivity of ULE (both mirror surfaces) at grazing angle of incidence for 0, 1, and 5 nm rms surface roughness at 1 keV [4].

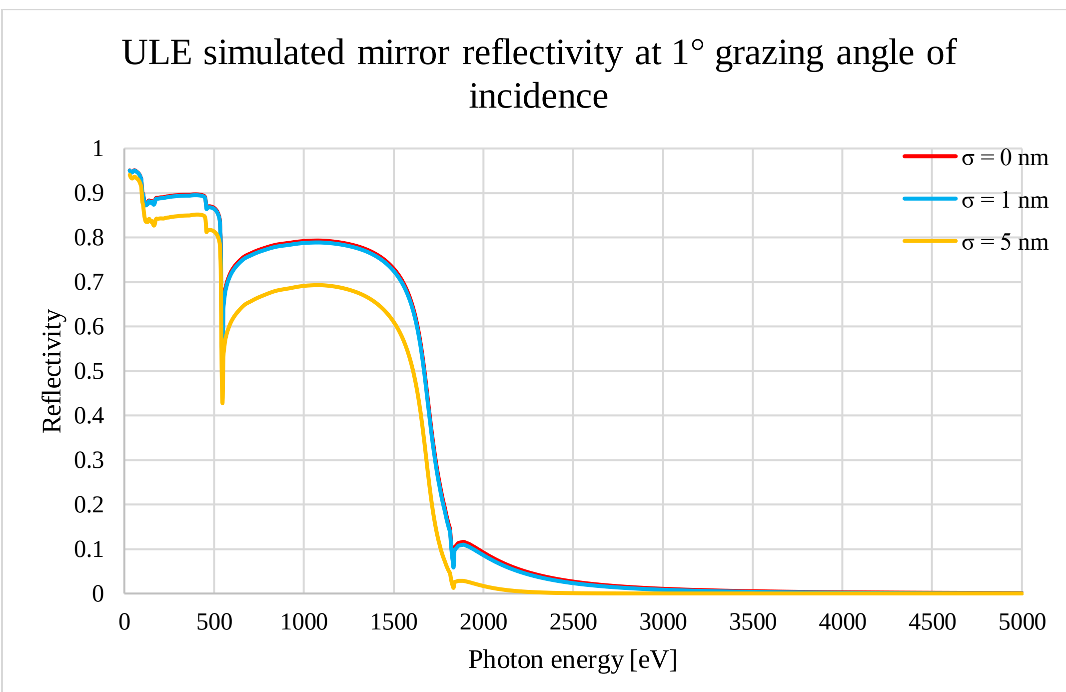

Figure 6. Simulated table showing mirror reflectivity of ULE at 1° grazing angle of incidence for 0, 1, and 5 nm rms surface roughness [4].

1.2 Ultrafast laser processing techniques

The ultrafast laser techniques performed on the transparent substrates used in the experiments for this thesis stem from ultrafast laser stress figuring (ULSF) techniques designed for accurately deforming thin mirrors [6]. ULSF uses an ultrafast laser focused into a substrate to induce a stress state to deform the substrate into a desired shape without introducing mid-spatial frequency errors or roughness [6]. Ultrafast laser assisted chemical etching was used to fabricate the samples for the experiment. This process is when ultrafast laser inscription is used to modify the substrate first, then chemical etching removes the laser modified material [7]. The deposition of optical energy is able to induce highly localized modifications into the substrate material, while not affecting the surrounding material [7]. When this process is combined with chemical etching, removal of material from a bulk glass substrate becomes an enabling technology for precise glass fabrication. When practiced on fused silica or ULE, the formation of periodic nanoplanes, or nanogratings, arise after laser writing [7]. These nanogratings are aligned perpendicular to the laser polarization direction and allow the etchant to quickly penetrate along the axis parallel to the gratings, but slowly in the perpendicular direction [7]. The success of using potassium hydroxide (KOH) as an etchant with fused silica substrates, like the high etching selectivity results seen in Figure 7 from Ross, et al [7], means that precise geometry in glass substrates can be achieved.

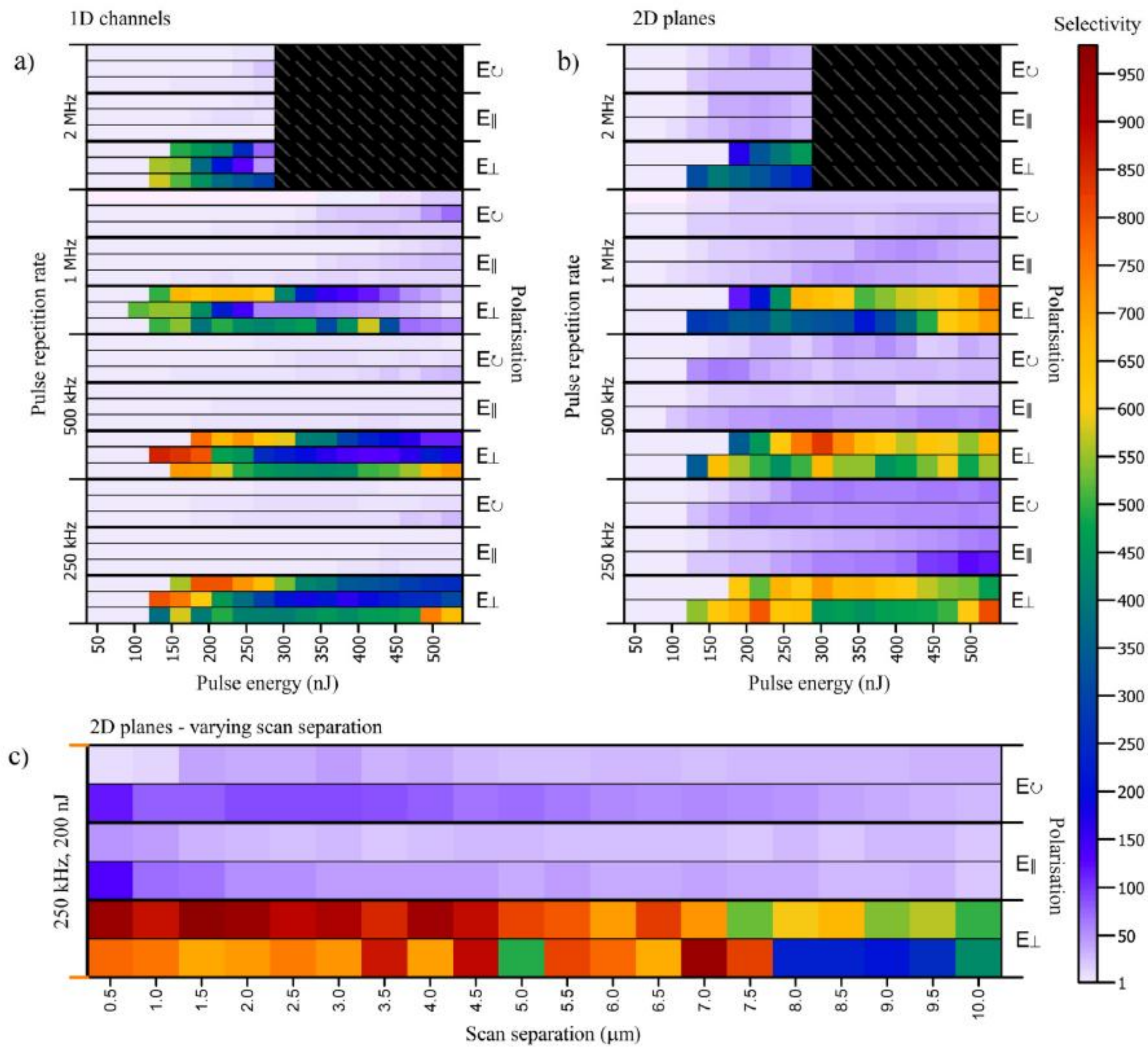

Figure 7. Heatmaps showing etching selectivity of laser irradiated material etched in an 8 mol/L KOH solution at 85 C. a) Selectivity of 1D channels – each triplet row (from bottom to top) corresponds to writing depths of 250, 500, and 750 µm in fused silica. b) Selectivity of 2D planar surfaces – each pair of rows correspond to etchant penetration into near (bottom) and far (top) surfaces of the substrate. c) Selectivity obtained for 2D planar surfaces as a function of scan separations. Pulse energy and repetition rate were kept constant at 200 nJ and 250 kHz respectively [7].

ULE behaves similarly to fused silica in regard to stress associated with repetition rate [8] and is the ideal glass to use for x-ray optics. While fused silica and ULE are compatible with ULSF, ULE can be slumped for x-ray optics fabrication and would perform better as a space flight optic. In the case of fabricating x-ray mirrors, slumping would be followed by polishing and ULSF.

Slumping is a simple and low-cost method that can achieve a desired mirror shape well enough for space missions, an example used for NuSTAR is seen in Figure 8. The x-ray mirrors of the NuSTAR observatory that launched in 2011 was constructed by slumping thin glass sheets to create the desired shell shape [9].

Figure 8. Illustration of slumping process: A thin glass sheet is placed on top of a cylindrical mandrel in an oven. As the temperature increases to about 600 °C, the glass softens and conforms to the shape of the mandrel [9].

In literature, primarily called laser-induced periodic surface structures (LIPSS), nanopillars have been able to create an anti-reflection coating for visible wavelengths when created on glass surfaces. This idea mimics the unique and natural phenomenon of antireflective properties found on the wings of the glasswing butterfly and numerous cicada species [10]. The biomimetic subwavelength structures have been replicated to restrain surface Fresnel reflectance for high transmission [11]. To increase the transmission of a transparent substrate, the effective index of refraction can be changed in a gradient-like way from the air to the substrate [11]. The AR properties being replicated from those found from the subwavelength structures in nature are replicating this change of refractive index from air to the root material, seen in the comparison below.

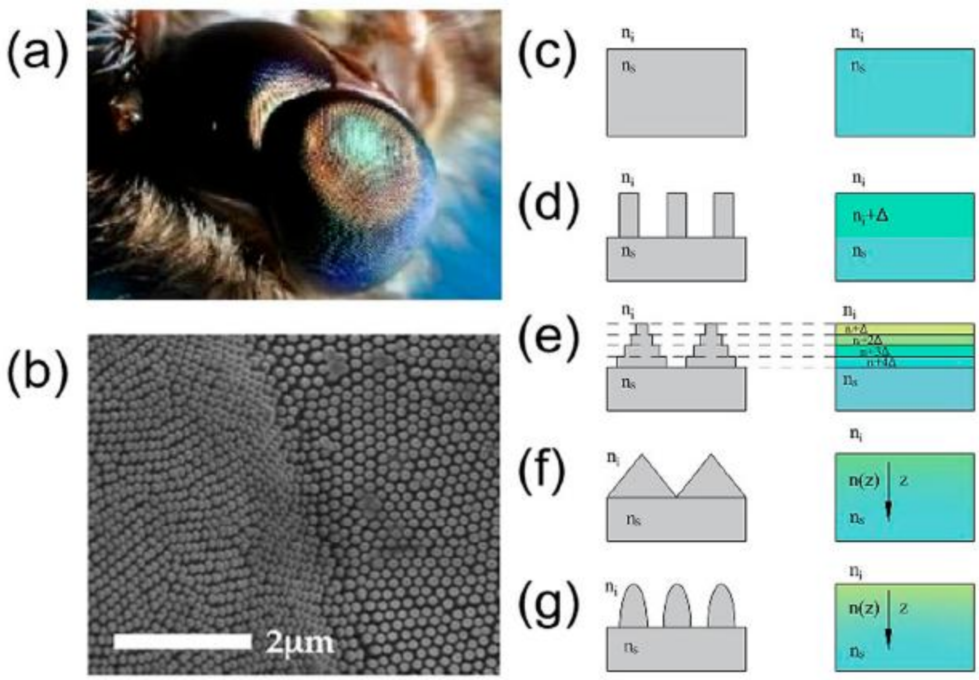

Figure 9. Biomimetic surface structures and refractive index gradient images. a) Moth eyes. b) scanning electron microscope (SEM) image of ommatidia (individual units of the eye). c) flat substrate. d) 1D grating surface. e) multilevel surface profile. f) continuous conical surface profile. g) continuous parabolic conical surface profile [11].

Pillar-like morphology has been applied to fused silica glass surfaces using circularly polarized ultrashort laser pulses. The laser-processed glass demonstrates antireflective properties in the visible with smaller than 1% reflectivity for various angles of incidence [10]. This antireflective laser-produced technique proposes a simple, low-cost, and chemical-free way of applying an AR coating that is commercially scalable and stable long term [10]. The following images were reported by Antonis Papadopoulos, et al. [10] in their work of direct laser fabrication of biomimetic omnidirectional antireflective glass surfaces. Comparing the natural forming nanostructures found on the wing and the laser-induced nanostructures, this suggests that replicating the antireflective properties of the wing is a promising solution to AR coating applications on transparent glass.

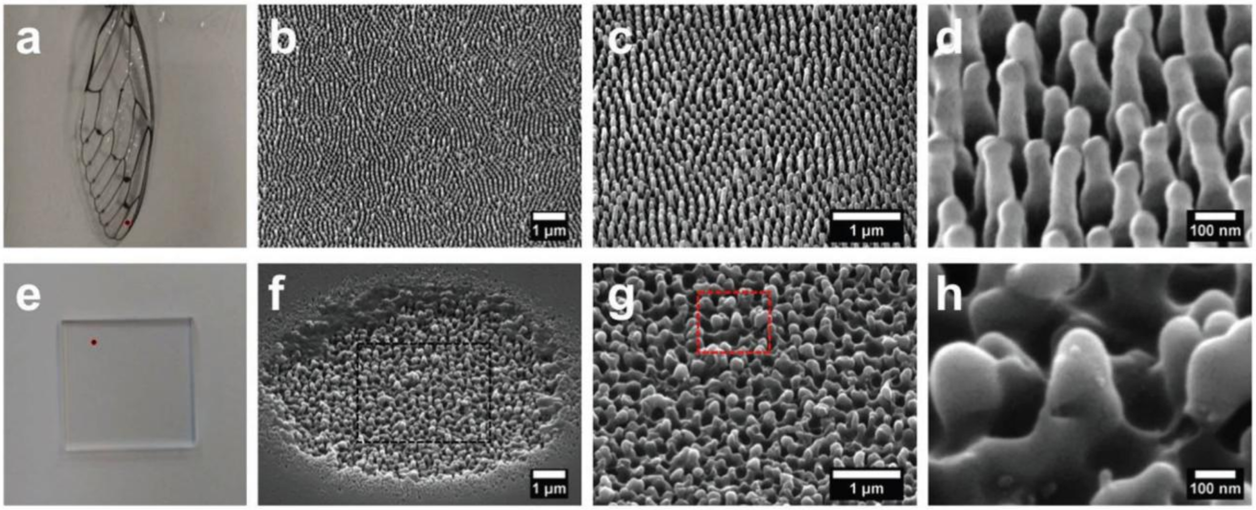

Figure 10. a-d) Photograph of a cicada wing with respective SEM images at different magnifications. e-h) Photogrpah of a fused silica plate and SEM images of the lasered spot. [10]

Chapter 2 – Surface Roughness of Fabrication Techniques

2.1 Motivation

An ideal x-ray telescope system uses lightweight and highly reflective mirrors. This can be achieved by using glass for those mirrors. Segmented optics made of glass can split the typical mirror shell into parabolic and hyperbolic segments. This allows for lightweight mirror stack to be used and nested densely. Fabricating these glass mirrors and maintaining the smooth surface roughness would ideally be to slump the glass to the desired shape [1]. To achieve the desired size of the mirror to slump, chemical-assisted laser etching of a larger sample may be required. Chemical-assisted laser etching induces less stress on the substrate than cleaving or grinding to remove excess material. Slumping and chemical-assisted laser etching are two processes necessary to achieve the desired size and shape for an x-ray optic, but their effect on contributing positively or negatively to surface roughness on ULE is unknown.

Potassium hydroxide (KOH) was used in selective laser etching of smaller samples from 100 mm diameter 1-mm thick and 50.8 mm diameter 0.375-mm thick ULE wafers. KOH has been found to be a significant chemical to use when ultrafast laser etching fused silica [7] as it allows for cleaner edges at the break and reduces fractures at the edge. This is especially helpful if one were to laser-etch irregular shapes from the wafer for the purpose of fabricating flexure-supported x-ray optics.

Results of KOH etching on surface quality of fused silica optics are better overall than HF/NO_3 when using high power lasers [12]. KOH efficiently passivates scratches on polished fused silica optics and has demonstrated maintaining or slightly reducing the surface roughness values before etching on fused silica [12]. Because ULE and fused silica are found to have similar qualities, similar results are expected.

2.2 Methods

2.2.1 Experimental Plan

An ultrafast laser with a wavelength of 1030 nm, a repetition rate of 100 kHz, pulse energy of 2 μJ, velocity of 25 mm/s, pulse duration of 350 fs, and a layer spacing of 1.5 μm was used to create the laser-written pattern on the wafer. A 0.25 NA objective using circular polarization was used. The chemical etching bath was prepared by combining stock KOH pellets with reverse osmosis (RO) water to a molar concentration of 8 mol/L. This solution was heated using a hot plate to 85 °C before placing the laser-etched wafer in the bath for 6 hours. The resulting wafer separated the smaller samples from each other with no visible fractures.

CAD was used to design the sample pattern on the 100 mm glass wafers so that the laser system could write it into the substrate. The wafer pattern included four 1-inch diameter wafers with 10 mm long flats and eighteen 10 mm x 10 mm squares nested inside leaving about 0.5 mm from the edge of the wafer to any sample. Each of the 10 mm x 10 mm squares had a number assigned to be etched at the midplane of the sample to not induce any stress or change the profile of the surface. There were two iterations of this experiment, and six of the eighteen square samples had two flexure-like features designed on the left side of the squares to be etched through the samples, seen in Figure 13. Because control samples needed to be remained unprocessed, the entire wafer was not etched. Instead, the 100 mm wafer was cleaved at the boundary of samples to be etched and samples to produce unprocessed samples.

Ultrasonic cleaning technology introduces high-intensity sound waves into a liquid that alternates high and low pressure throughout the liquid [13]. The changing pressure may cause a small bubble to form near a contaminant on the surface of a sample being cleaned, effectively dislodging the contaminant from the surface [13]. Prior to some of the 10 mm samples being etched, they were cleaned using an ultrasonic cleaner submerged in 1 liter of 1% concentration of Liquinox for 30 minutes at 60°C, then in 1 liter of 1% concentration of Citranox for 30 minutes at 40°C. The samples were cleaned off with RO water and nitrogen gas. Ultrasonic cleaning allows sub nanoscale contaminants to be removed without contacting or inducing damage to the surface [13]. This method of ultrasonic cleaning was also performed in between etching and taking surface roughness measurements.

Two iterations of this experiment were performed, the first on 0.375 mm thick ULE with a looser tolerance of closer to 1 nm rms surface roughness, and the second on 1 mm thick ULE with a smaller surface roughness of 0.5 nm rms. Iteration 1 was necessary because samples were readily available.

Iteration 1 (Figure 11) consisted of two controls, two etched, and two slumped 10 mm x 10 mm square ULE samples. The slumped samples underwent a thermal cycle in a temperature controlled thermal chamber. This batch of samples were measured after undergoing slumping and etching with a white light interferometer (WLI) also known as coherent scanning interferometer (CSI), and an atomic force microscope (AFM) discussed later. Each sample was measured in four corner regions to average the surface roughness effects from each fabrication technique, see Figure 13 below for measured regions. The control samples for this iteration were simultaneously thought of the 'before' surface roughness measurement for the slumped and etched samples as no before-surface measurements were made of slumped and etched samples.

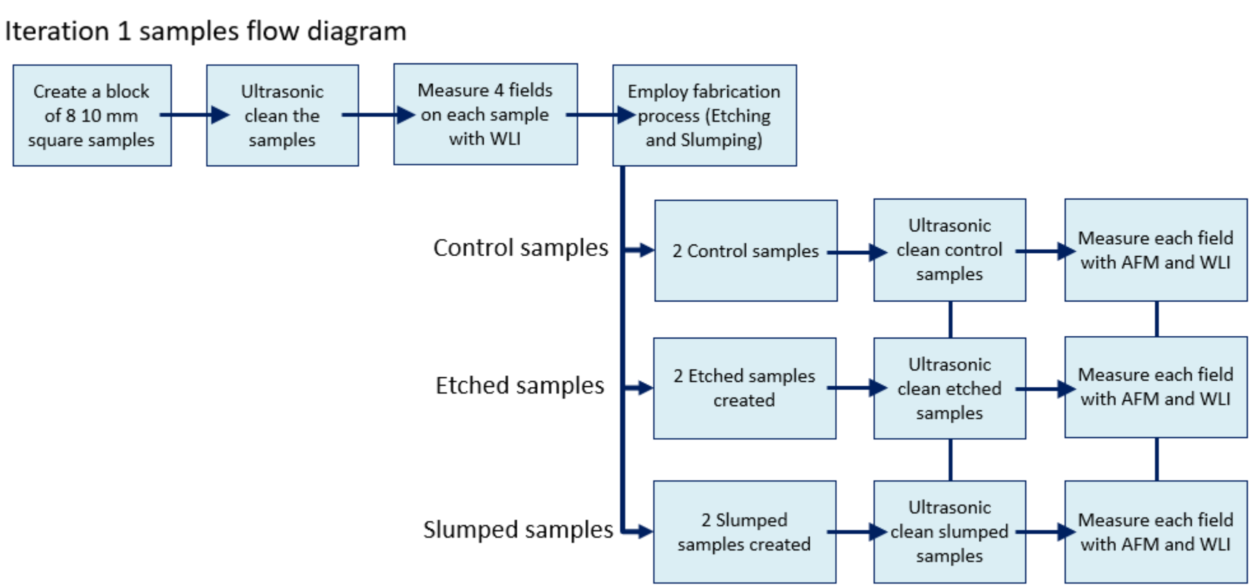

Figure 11. Process flow diagram of Iteration 1 samples.

Slumping is one of the fabrication techniques for creating the desired shape of an x-ray mirror as discussed previously (see Fig 8). The slumped samples for iteration 1 were not physically slumped using a mandrel to change the shape of the samples, but just thermally cycled. This meant that 2 of the 10 mm squares were placed in a temperature-controlled oven to simulate the effects that slumping has on a ULE substrate.

Iteration 2 (Figure 12) consisted of four etched and four controls of 10 mm x 10 mm square ULE samples. The 1 mm thick ULE used for these samples was initially smoother than the ULE used for iteration 1. Slumped samples were not created for this iteration due to a change in the fabrication plan. X-ray mirrors fabricated from glass would undergo polishing after slumping, so surface roughness arising from the slumping process was no longer critical to quantify. The etched samples underwent the same etching parameters as iteration 1, but AFM and WLI measurements of the surface roughness were recorded prior to etching for better comparison. The etched and control samples were measured in the same fashion as iteration 1 using the AFM and WLI after cleaning the samples after etching. A simplified flow chart of the experimental process of iteration 2 samples is shown below.

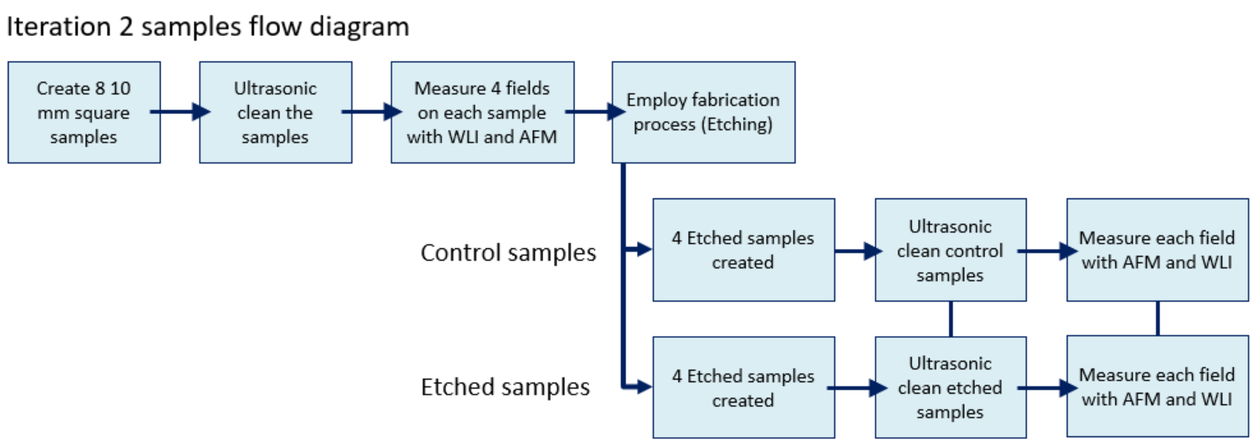

Figure 12. Process flow diagram of Iteration 2 samples.

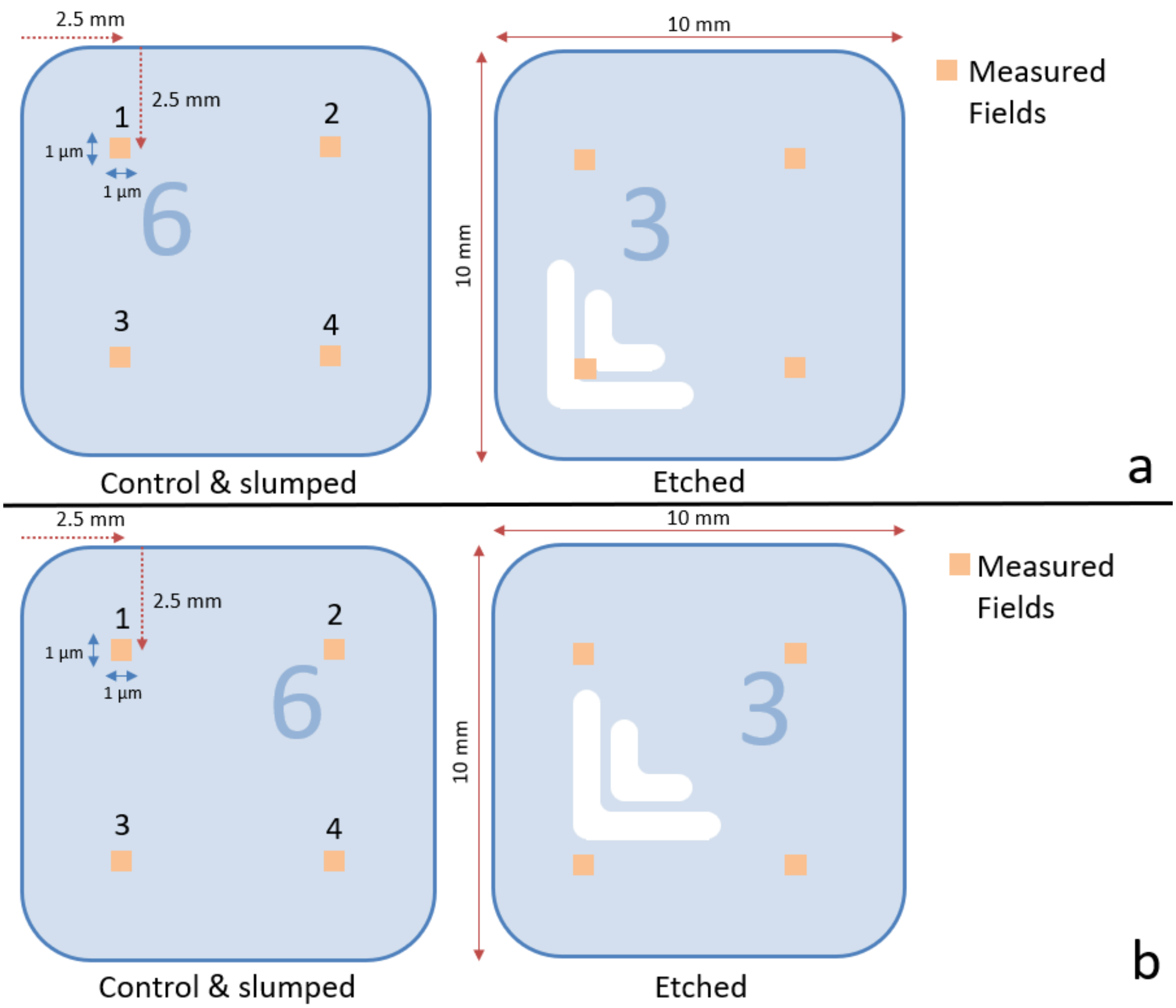

Figure 13. a) Samples created and used for the first iteration of the experiment. b) Samples created and used for the second iteration of the experiment, note the flexures moved up to make measuring easier. 1 µm x 1 µm area was used for AFM measurements. WLI measurements used 0.17 mm x 0.17 mm in approximately the same locations.

Field measurements were taken of iteration 1 samples using the WLI before and after surface processing. AFM measurements were taken of iteration 1 samples only after surface processing in hopes of higher resolution of the surface roughness. Iteration 2 samples were measured before and after surface processing with both the WLI and AFM for complete comparison of surface roughness changes. Based on the higher resolution of roughness measurements with the AFM observed with iteration 1, the AFM became the primary instrument to compare surface roughness effects for iteration 2.

2.2.2 Atomic force microscope (AFM)

An atomic force microscope provides nanoscale profiles in 3 dimensions by measuring forces between a sharp probe and a surface in a short distance (nanometer separation) [14]. The small sharp probe tip on the cantilever uses raster scanning across the surface to measure in two dimensions. A Park Systems NX20 AFM in tapping mode was used for measuring the samples in this experiment, so the cantilever moves at a high amplitude of oscillation just above the surface. This AFM is also equipped with low-noise Z detectors, producing a noise of 0.02 nm over a large bandwidth. When the tip approaches the surface, attractive forces between the tip and the surface cause the cantilever to deflect towards the surface, but simultaneously increasingly repulsive forces deflect the cantilever [14]. The basic working principle of an AFM can be seen in Figure 14 below. Tapping mode (also known as intermittent contact) works best when the surface to probe tip separation is in a range of 0.5 to 2 nm [14]. This mode also leads to less likelihood of contamination of the sample under test. Two other modes are available: contact mode and non-contact mode. Contact mode requires the probe almost contacting the surface of the sample and is ideal when the surface to probe separation is less than 0.5 nm [14]. Non-contact mode is used when the surface to probe tip separation is between 0.1 to 10 nm [14]. For these experiment iterations, because the surface roughness is expected to be near 0.5 nm rms, the probe tip to surface separation is expected to be slightly greater than 0.5 nm, hence tapping mode was used.

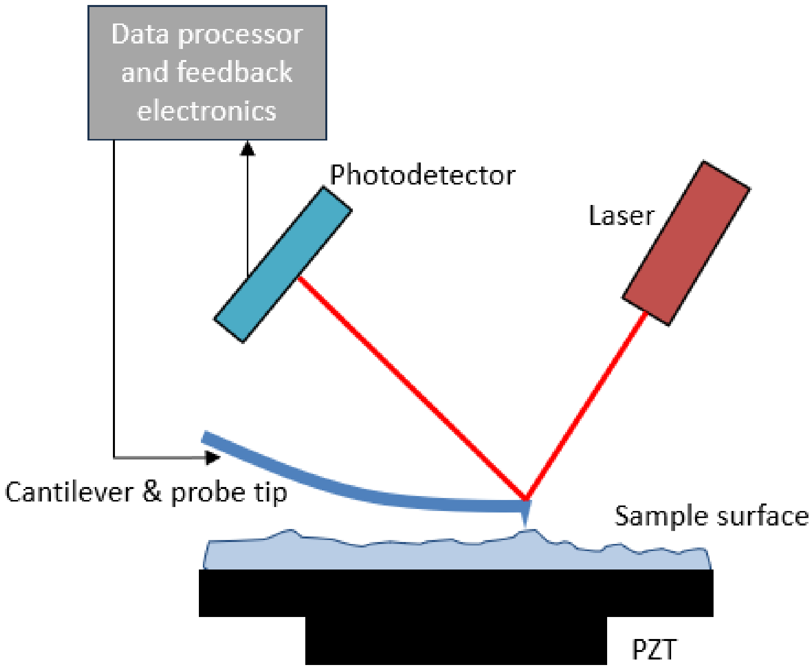

Figure 14. Basic AFM depiction

The AFM parameters used to measure each of the four fields on the samples were 1 µm x 1 µm measured area at 1 Hz scan rate, about 2 nm/s, so each image measured 256 pixels. Each scam took about 4 minutes to acquire.

The 1 µm x 1 µm images taken with the AFM result in files encoded with 3-dimensional data. Gwyddion is an open-source software designed specifically for scanning probe microscopy (such as AFM) analysis [15]. It is designed to provide fast and reproducible data-processing techniques for its users by having basic operations available for successful evaluation of obtained data [15]. The key features used for data analysis of the AFM images for this experiment were: data filtering by mean plane subtraction, instrument tilt plane leveling, correction of image defects by line correction, and false-color representation of the image. In some cases, obvious artifacts were captured in the image collection, so a mask was used to ignore outliers for the rms surface roughness. Once analyzed, the ‘RMS Roughness (Sq)’ was viewed in Statistical Quantities. The figure below shows an example of an AFM image before and after processing of a control sample.

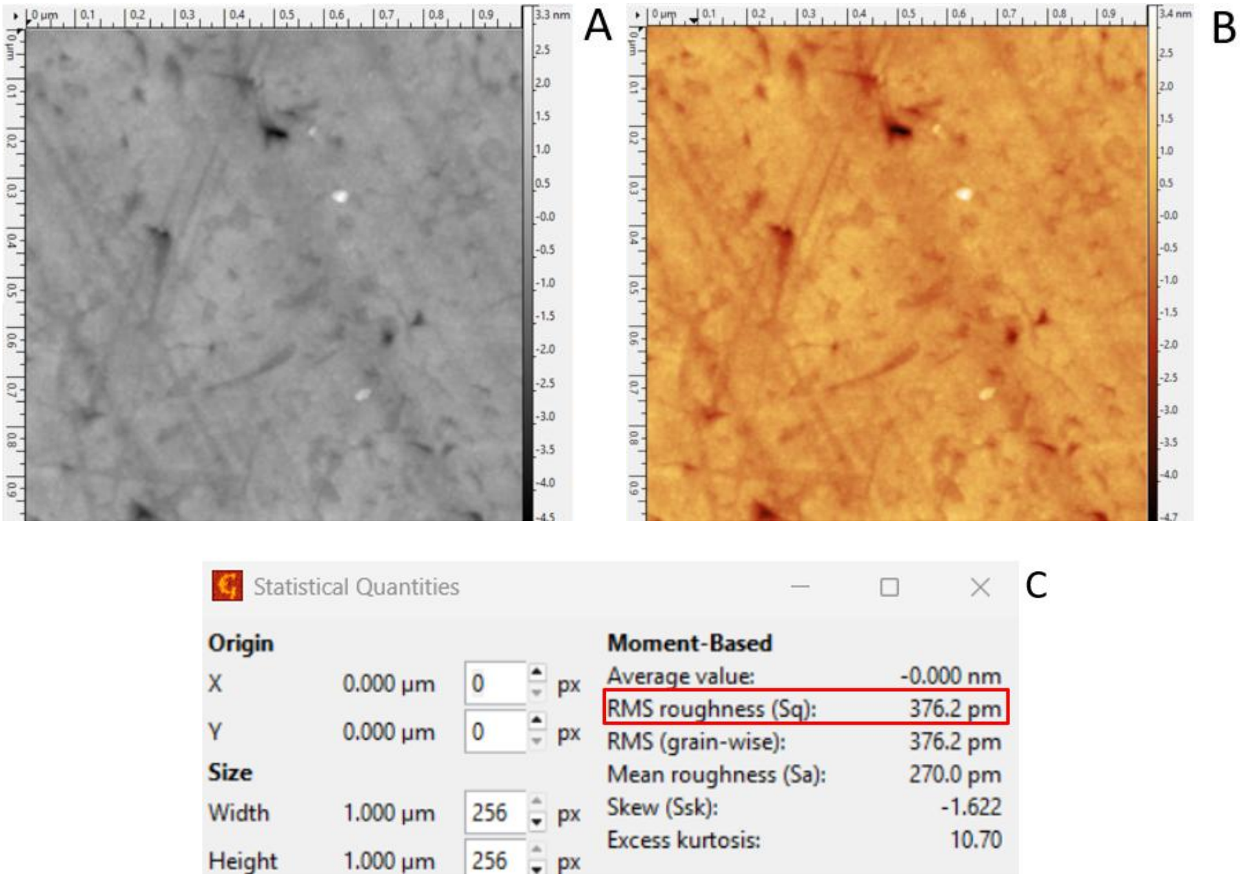

Figure 15. a) Raw AFM image file of unprocessed ULE surface from iteration 1. b) Processed AFM image file of unprocessed ULE surface from iteration 1. c) Statistical Quantities in Gwyddion used to identify rms surface roughness.

Each field for every sample was evaluated in this way before and after being exposed to surface processing (etching or slumping). Then the average value and standard deviation was found from all fields measured for etched samples, control samples, and slumped samples for both iterations of the experiment.

2.2.3 *White-light interferometer (WLI)*

The Zygo NewView white light interferometer is another instrument used to measure the surface topography of a unit under test. Using a broadband source for interferometry uses a short coherence length to determine height variations across a sample [16]. Broadband illumination is important for interferometry when measuring the shape of rough surfaces because the short coherence length only allows interference fringes to form within a narrow region near the surface. This contrasts monochromatic light sources in interferometry due to fringes being able to be seen for a much larger region. A Zygo NewView WLI uses a two-beam Mirau interferometer at the microscope objective to measure the height variations or surface roughness of a sample. It is equipped for surface topography repeatability of 0.08 nm for all magnifications as it produces the same resolution regardless of NA [17]. A Mirau is a variation of a Michelson interferometer specifically designed to integrate with microscope objectives in a vertical overlapping configuration. Source light that is reflected from the test surface interferes with the reflection from the reference surface and creates an interference pattern imaged and digitized to the computer output [16]. A Mirau type of interferometer is typically used with magnifications between 10x and 50x or 0.82 mm x 0.82 mm and 0.17 mm x 0.17 mm, respectively. This schematic can be seen in Figure 16 below.

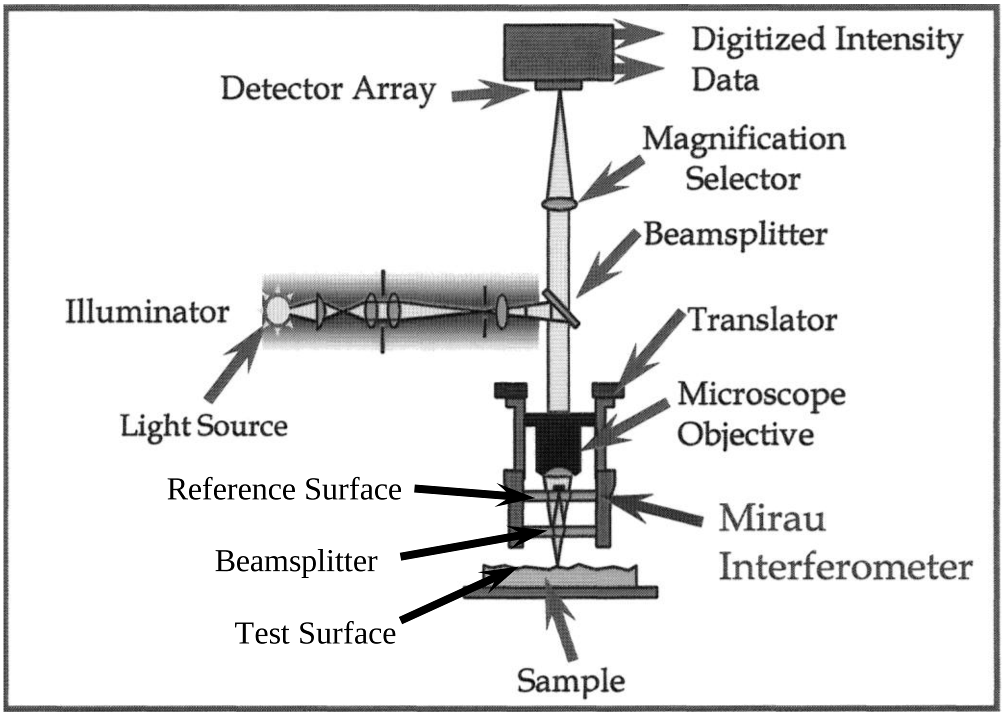

Figure 16. Optical schematic of WLI microscope [16].

Drawbacks of the WLI are its low spatial frequency limitations as it becomes limited by the NA available which causes limited spatial resolution by the Rayleigh criterion for fields smaller than 100 microns [18]. The AFM has capabilities to measure roughness in the high-spatial frequency range and overlaps slightly into the mid-spatial frequency range which is where the WLI is best for [18]. Both instruments were used to measure the surface and compare which instrument provided better results for the samples tested. Using the WLI made for much quicker data collecting than the laborious AFM. The WLI was set to use a 0.55 NA (50x) objective measuring four 0.17 mm x 0.17 mm fields in approximately the same region as the AFM measurements.

2.3 Results

2.3.1 Surface quality and power spectral density (PSD)

The surface quality on a work piece is a measure of surface perfection after cleaning and processing [15]. In this case, the surface quality is dependent on chemical interactions on the surface, any foreign or unwanted particles, and subsurface damage. Surface roughness is the metric to describe the topographical relief of a surface and can be described on the angstrom to nanometer scale length, great for optically smooth surfaces [19]. Roughness, δ, is generally quantified by the root mean square (RMS) of the surface topography:

$$\delta = \sqrt{\frac{1}{N}\sum_{i=1}^{N} z_o^2} \tag{2}$$

where N is the number of discrete, equally spaced measured points on a surface, and z_o is the local surface height above or below the mean height of the surface [19]. The computed RMS is dependent on the total length of the surface profile (maximum spatial length), the surface area being average over, and distance between data points (minimum spatial-scale length) [19]. Depending on the measurement technique, RMS of the same surface can vary, as seen later between WLI and AFM measurements. Other common quantities of interest are mean roughness (Sa), maximum height range (Sz), and rms roughness (Sq).

To describe the surface roughness completely, the power spectral density (PSD) function is observed. The PSD is the spatial frequency spectrum of the surface roughness measured in inverse length units calculated from the square of the magnitude of the Fourier transform of the surface height data (z_o) [19]. Power spectra are useful ways to describe optical surfaces due to their relationship to the scattering per unit solid angle from a surface [19]. WLI measurements typically fall into the μ-roughness scale or mid-range spatial scale, and AFM measurements extend into short-range spatial scale near almost sub-μ scale [19]. The figure below shows the various spatial-length scales.

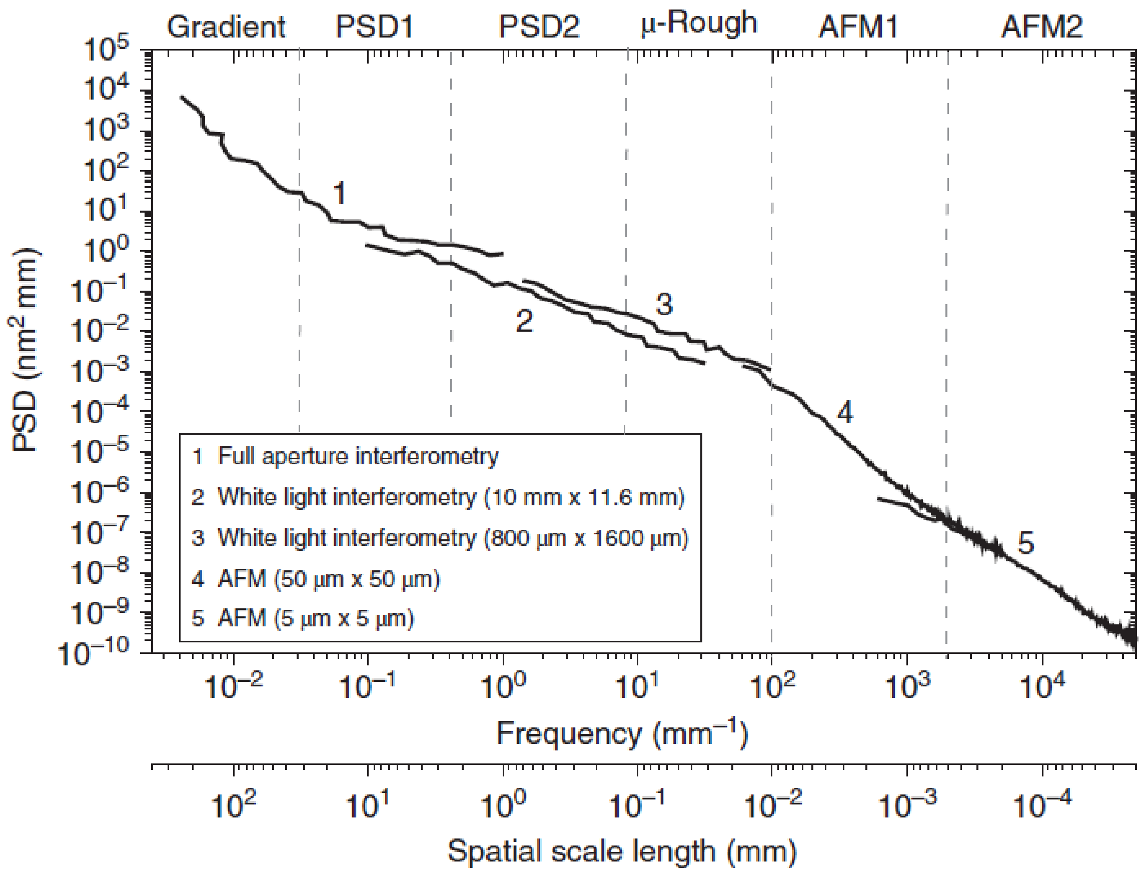

Figure 17. Example of a composite power spectral density of an optical surface across different spatial scale lengths using different measurement techniques [19].

Gwyddion has capabilities to create power spectral-density function plots and values given the 3-dimensional images [15]. A PSD plot covering the WLI spatial scale and AFM spatial scale was created from PSD data averaged from control samples and etched samples for iteration 2. For the AFM measurements, the data was extracted from Gwyddion by using the processed images and selecting the ‘Calculate 1D statistical functions’ icon and ‘PSDF’ for quanitity. One field whose surface roughness was closest to the average roughness from each sample of the etched and control samples from iteration 2 were analyzed. The data was generated by averaging the horizontal line scan profiles of each sample set by the AFM. This effectively created the spatial frequency achieved by the AFM for 1 μm x 1 μm measured fields.

For the WLI, PSD plots were recreated from .csv files extracted from PSD Analysis in Zygo’s Mx software. One field whose surface roughness was closest to the average roughness from each sample of the etched and control samples from iteration 2 were analyzed. 1D line scan profiles in x and y directions of the measured region were averaged to generate the spatial resolution achieved by using the WLI. Find the figures comparing iteration 2 spatial frequency of the AFM and WLI before and after fabrication processes below.

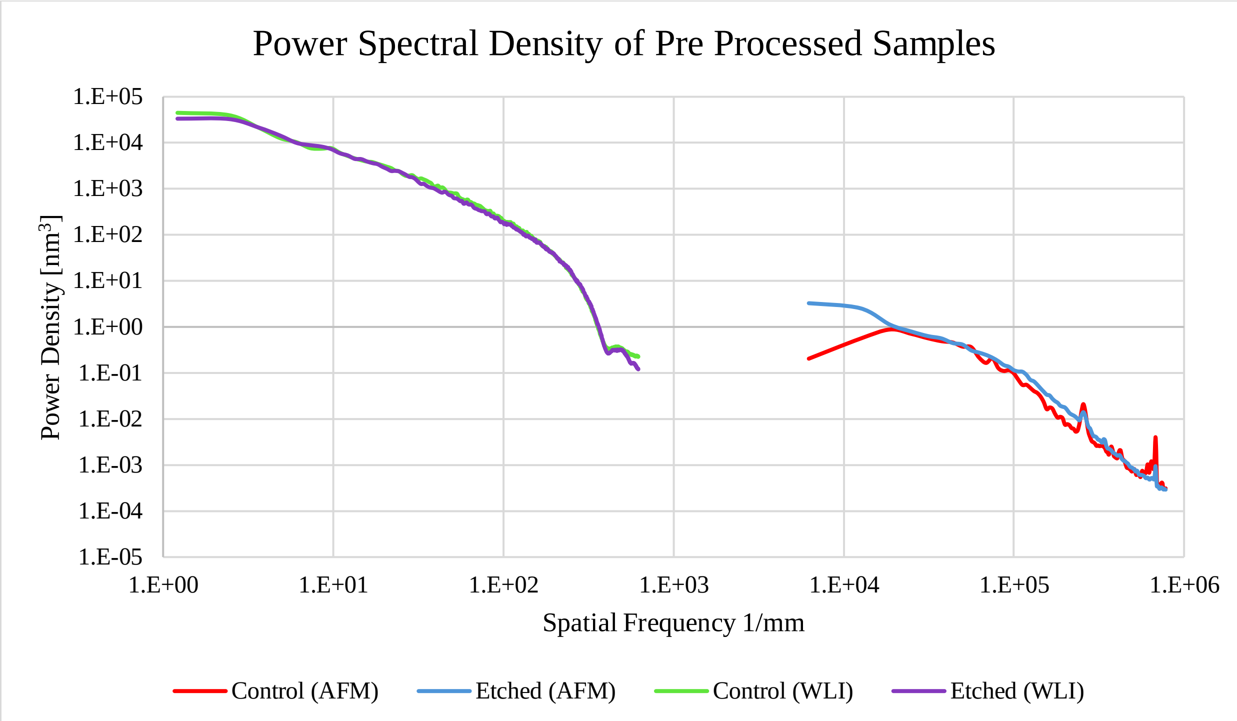

Figure 18. Power spectral density of pre-processed samples of iteration 2 (1 mm thick ULE) for WLI and AFM measurements.

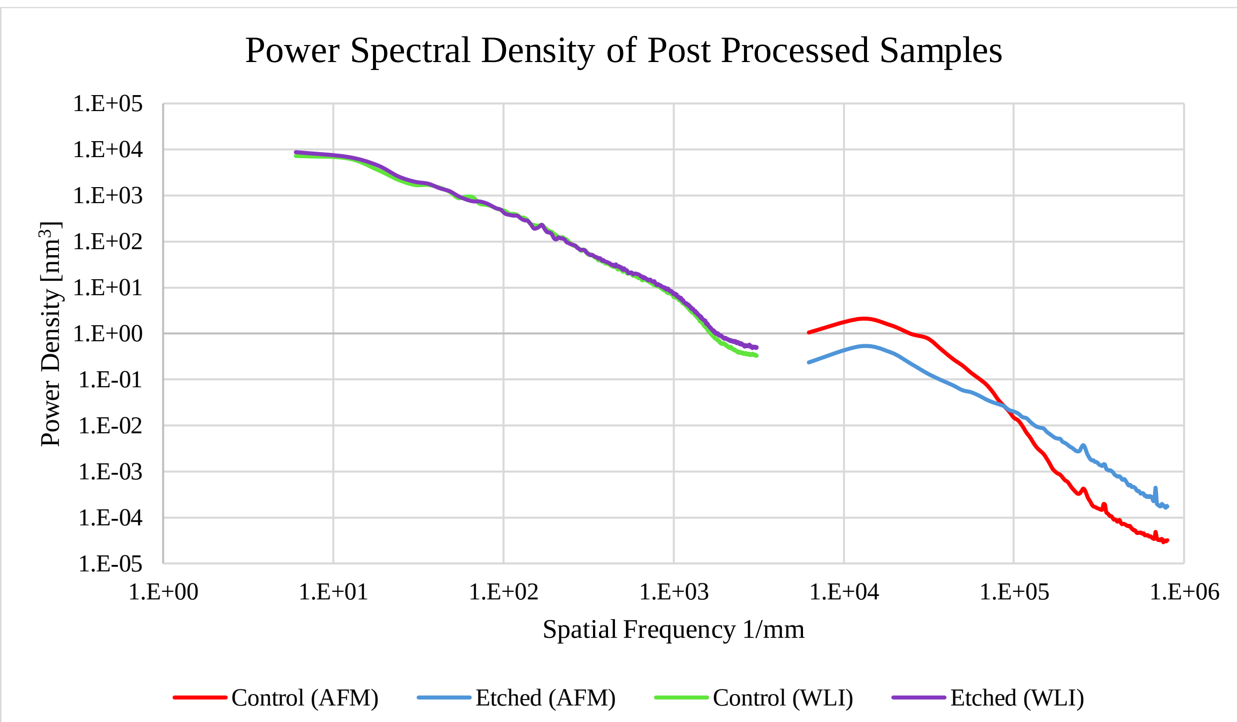

Figure 19. Power spectral density of post-processed samples of iteration 2 (1 mm thick ULE) for WLI and AFM measurements.

The lack of overlapping spatial frequencies of the PSD plots is due to the limited resolution of the NA from the WLI and the size of the measured fields. The reason that the spatial frequency shifted by almost a decade to the right with the WLI is due to the preprocessed samples being measured with the 10x objective with field size measuring 0.82 mm x 0.82 mm, whereas the post processed samples used the 50x objective making the field size 0.17 mm x 0.17 mm. The post processed field measured with the WLI was equivalent to 1000 pixels x 1000 pixels, where the AFM's 1 µm x 1 µm field was equivalent to 256 pixels x 256 pixels. This meant that 1 pixel in the WLI field was about 0.17 μm^2 and 1 pixel in the AFM field was about 0.004 μm^2. Even with the minimum field size possible to measure with the WLI, the spatial frequencies do not overlap with the AFM. The AFM however has the ability to measure larger fields, so to bridge the spatial frequencies between the WLI and AFM, the measured field size using the AFM could be increased to 5 µm x 5 µm.

The surface roughness of iteration 1 (0.375 mm thick ULE) was measured on the WLI before and after the fabrication methods were employed. Below is the resulting data for the roughness in nm rms for etched, slumped and control samples, where the 'x' represents the average, the horizontal bar represents the median, the shaded box represents the interquartile range, and the extended vertical lines represent the minimum and maximum values.

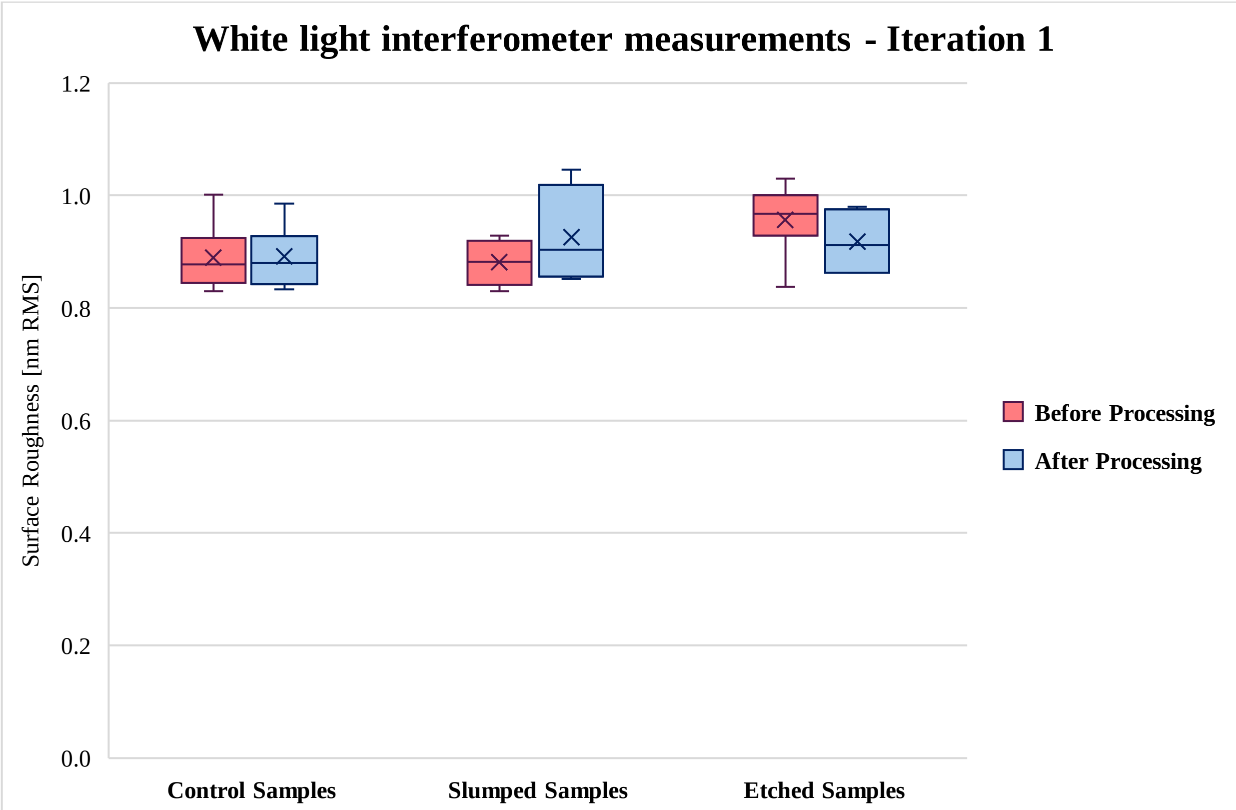

Figure 20. Surface roughness measurements using the WLI on iteration 1 samples (0.375 mm thick ULE). Four 0.17 mm x 0.17 mm fields were measured on each of 2 etched samples, 2 slumped samples and 2 control samples.

The AFM was used to measure the same samples of iteration 1 after the fabrication process, as seen in the previous PSD plots.

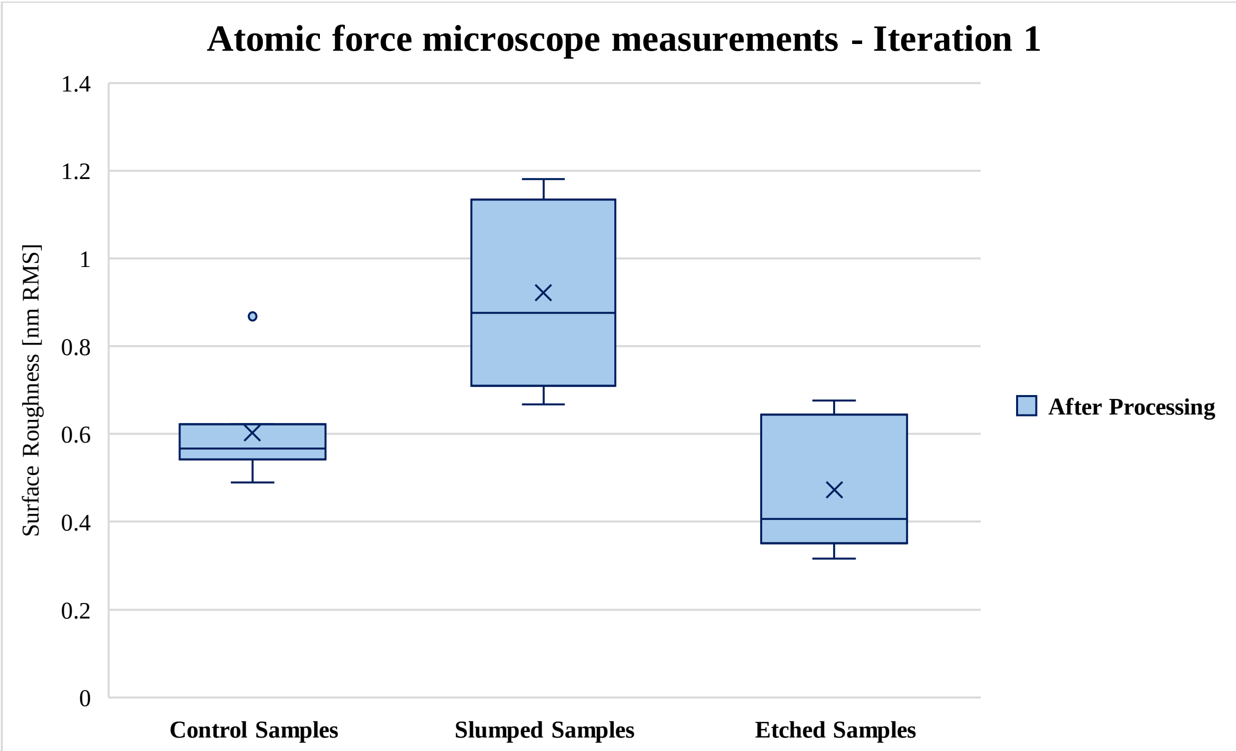

Figure 21. Surface roughness measurements using the AFM for iteration 1 samples (0.375 mm thick ULE). Four 1 µm x 1 µm fields were measured on each of 2 etched samples, 2 slumped samples and 2 control samples. (Note only measurements after processing were recorded)

Iteration 2 only consisted of control and etched samples. The surface roughness of the 1 mm thick ULE was measured with the WLI and AFM before and after surface processing.

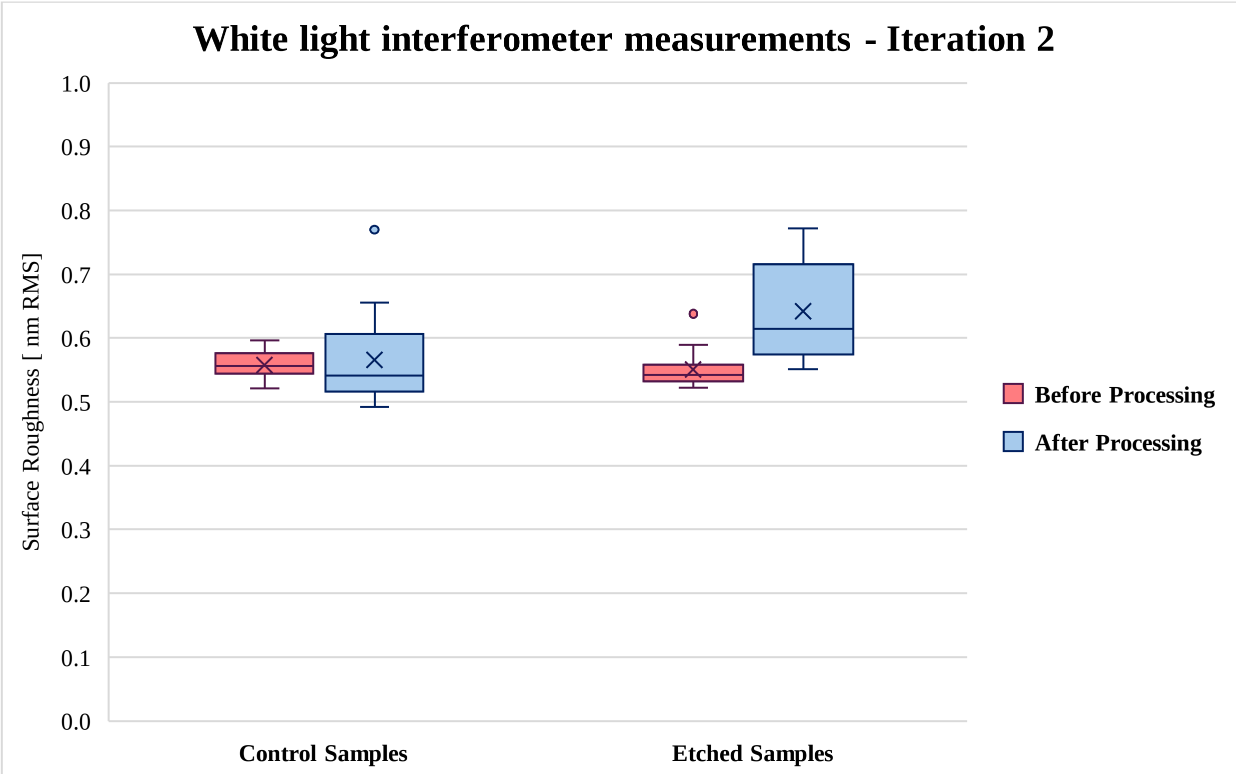

Figure 22. Surface roughness measurements using the WLI for iteration 2 samples (1 mm thick ULE). Four 0.17 mm x 0.17 mm fields were measured on four etched samples and four control samples. The small data points detached from the box plots are outliers in the data set.

The discrepancy between the WLI measurements of the etched samples may be due to residual KOH etching the polished surface of the sample. The timeframe for when the experiment was completed and when the last set of etched samples were measured with the WLI was about five months later than the measurements taken with the AFM.

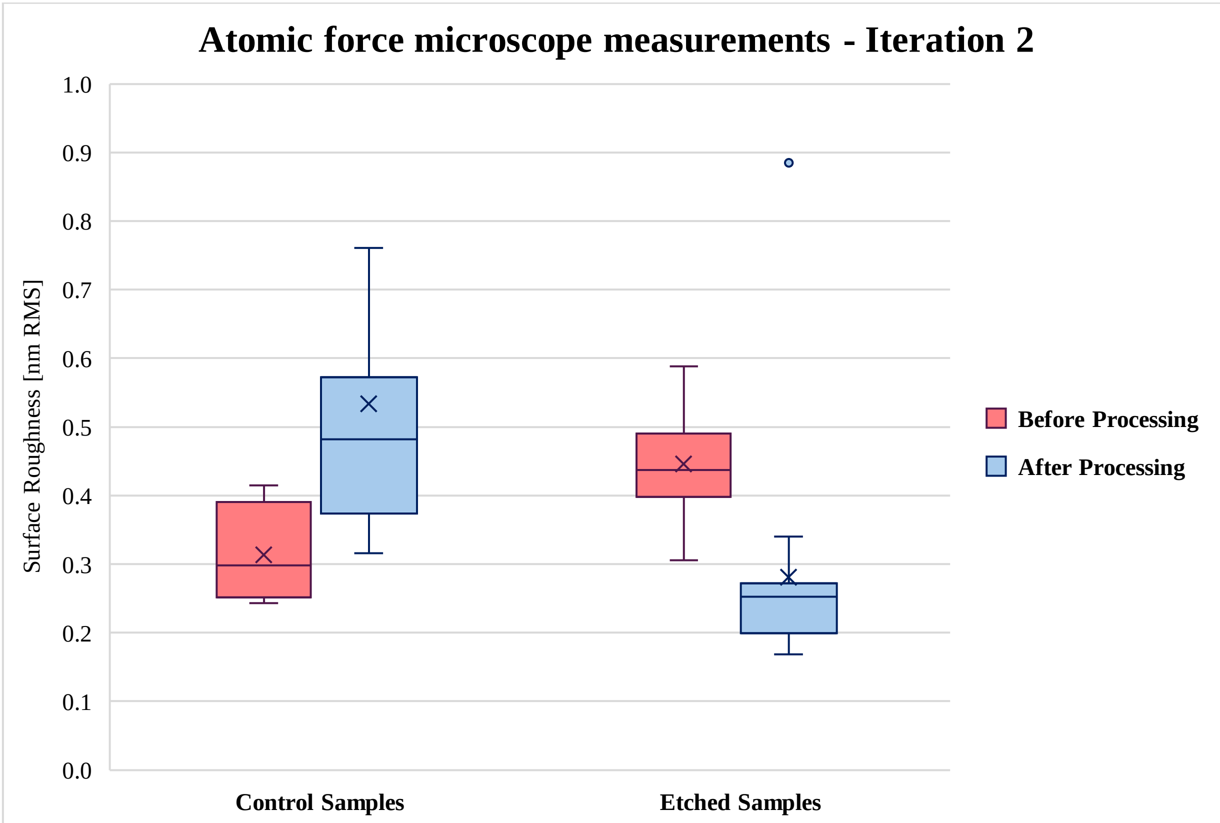

Figure 23. Surface roughness measurements using the AFM for iteration 2 samples (1 mm thick ULE). Four 1 µm x 1 µm fields were measured on four etched samples and four control samples.

2.4 Discussion

Visual results from taking surface roughness measurements with the WLI were not significantly different to being able to identify the difference between surface processes solely based on the RMS roughness of a measured field. With the AFM, however, each surface process had distinguishable characteristics that were identifiable at such a small scale. The control ULE samples in both iterations showed normal surface defects: scratches and polishing artifacts. Etching samples in both iterations demonstrated smoother surfaces (lower roughness values) and occasionally showed what appeared to be sub-nanometer deep periodic pits across the scanned area. Slumped samples appeared to show a rougher surface than the control having more scratch marks. Below are AFM image comparisons of iteration 1 and 2 of different surface processes.

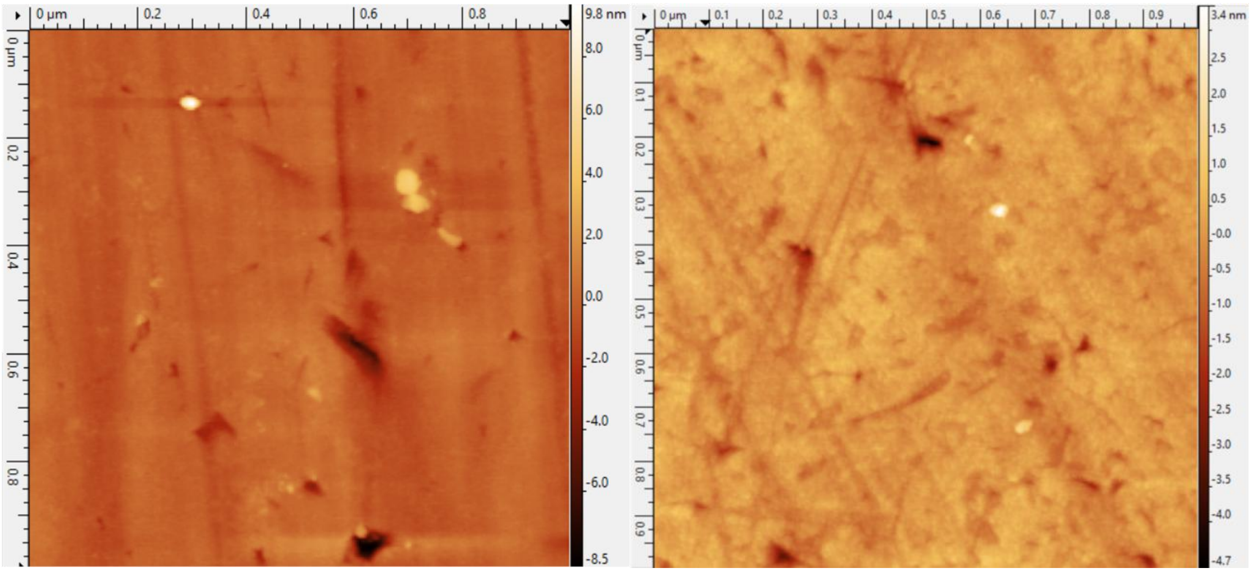

Figure 24. AFM images of control samples. Left: Iteration 1 measuring 0.577 nm rms. Right: Iteration 2 measuring 0.368 nm rms. Note the height is different for each iteration. Notice the similarity of the unprocessed ULE surface – both show polishing effects and some scratches.

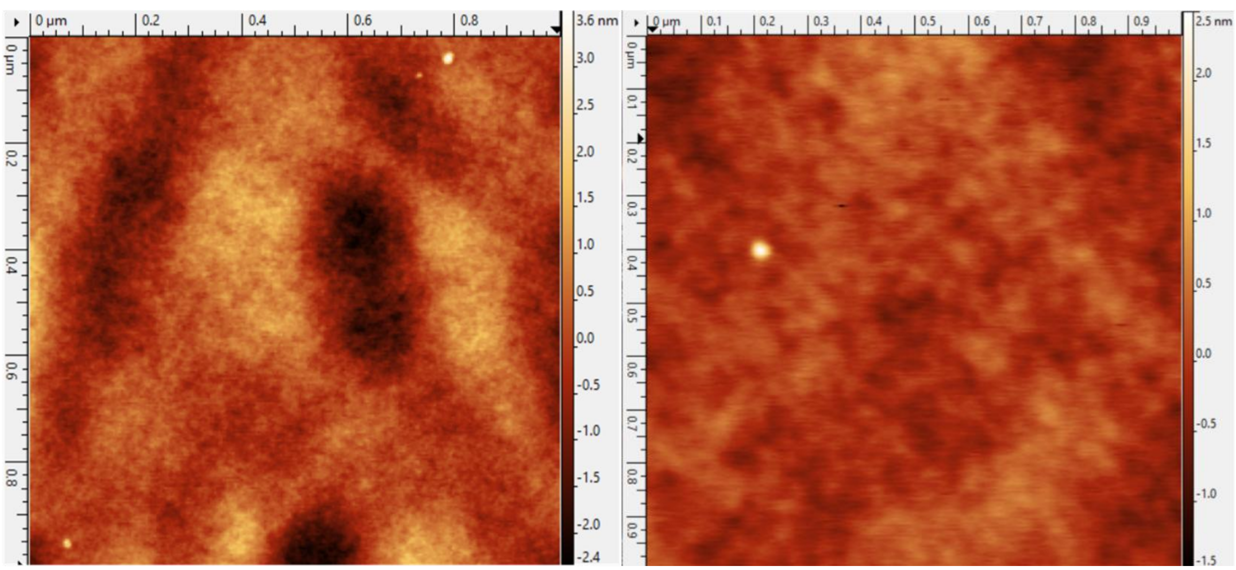

Figure 25. AFM images of etched samples. Left: Iteration 1 measuring 0.676 nm rms. Right: Iteration 2 measuring 0.259 nm rms. Note the height is different for each iteration. Notice the similarity of a 'fuzzy' image – both show some darker regions and some lighter regions.

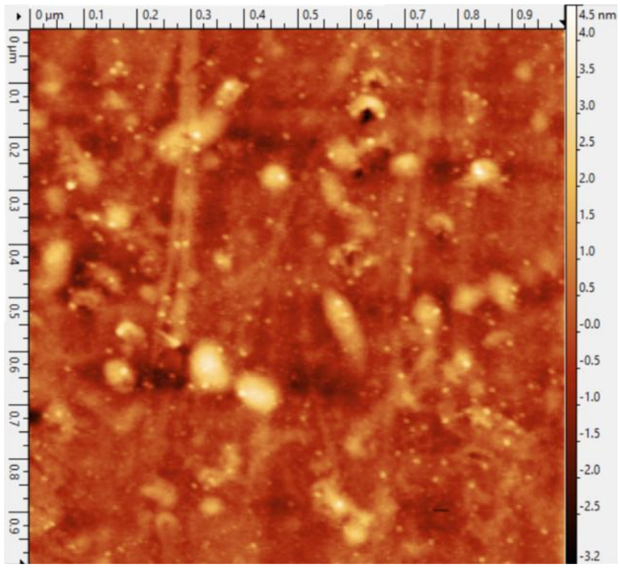

Figure 26. AFM image of slumped sample. Iteration 1 measuring 0.667 nm rms. Notice the stark difference between this slumping result compared to the unprocessed samples.

Slumped ULE substrates for the purpose of fabricating x-ray optics should be investigated further because only one iteration of slumped samples measured with the AFM is not sufficient to determine if slumping has a significant negative impact on surface roughness, or if it is highly dependent on the nominal surface roughness. Etching, however, does not appear to negatively impact surface roughness, and in some cases, can improve surface roughness, as seen in literature [12] and demonstrated through this experiment.

This experiment successfully demonstrated that KOH chemical assisted laser etching of ULE substrates for fabricating x-ray optics does not negatively affect the surface roughness and maintains the surface roughness requirement of 0.5 nm rms or less.

Future investigations of fabrication processes regarding surface roughness should include observing samples that have undergone both slumping and etching to replicate the process that would be followed for fabricating a real x-ray optic mirror.

Chapter 3 – Laser-Induced Surface Nanopillars

3.1 Motivation

An x-ray telescope bandpass is defined by the reflecting surface, typically a thin film coating of either single layer or multilayer [5]. Mirror or reflective coatings are employed in telescope optics to enhance the performance of most astrophysical x-ray missions [5]. The substrate that forms the body of the mirror is highly responsible for image quality. One of the many typical substrates that can reflect x-rays include fused silica, although not very efficiently on its own [5]. By adding a mirror coating, performance can be maximized but can also induce unwanted scattering. When the back surface is reflective, unwanted scattering of light can occur. An exaggeration of light traveling through part of an x-ray telescope is in Figure 27.

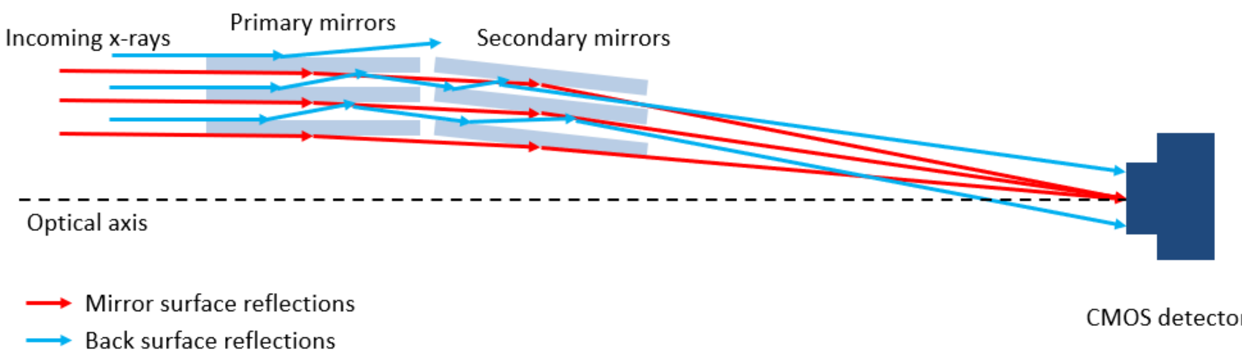

Figure 27. Depiction of desired reflections (mirror surface) and undesired reflections (back surface) of a cut view of an x-ray telescope.

With the nested mirror stack arrangement of x-ray telescope optics, scattering of light off the back surface of a substrate is undesirable and may interfere with performance. High performance in reflection and image quality is wanted from the front surface of the x-ray optic mirror given by the incident grazing angle of the x-rays, but the back surface, only about 1 mm away from the next mirror, should not be reflective in the x-ray band. When correcting the figure of the front surface of an x-ray mirror, it is done through the back surface. Minimizing back surface reflections improves the accuracy of front surface measurements when performed through the substrate, as it reduces interference and spurious signals that can distort the measurement. An example of this metrology schematic can be seen in Figure 28 where an interferometer could measure the reflecting surface.

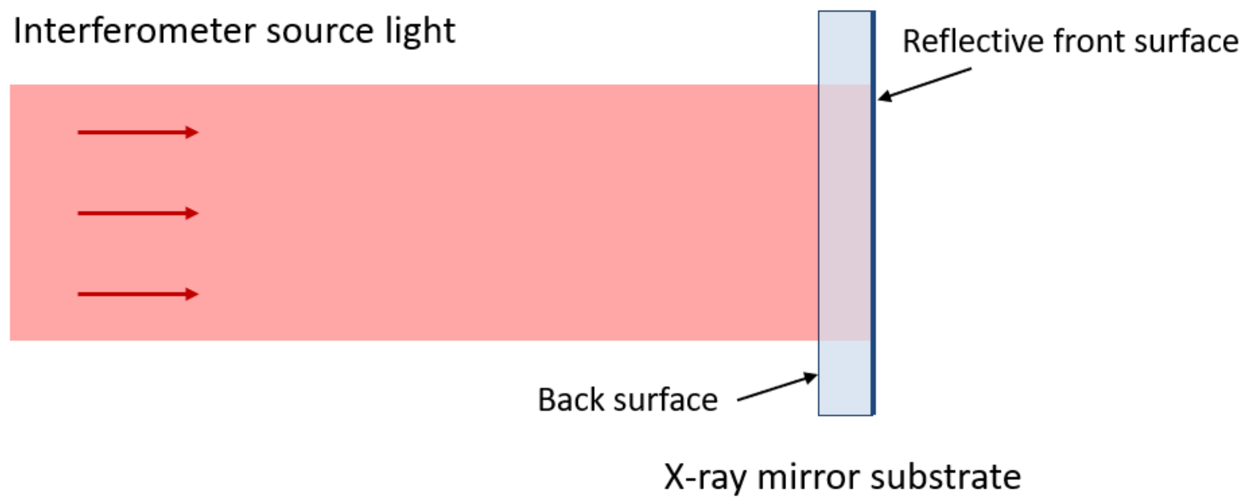

Figure 28. Diagram of metrology configuration where an interferometer is measuring the front surface of the x-ray mirror through the back surface.

The formation of laser-induced sub-wavelength anti-reflection (AR) coatings are inspired by the naturally occurring surfaces found in nature [20]. In nature, insects like the cicada or glasswing butterfly have arrays of sub-300 nm pillar-like structures that represent AR surfaces to help them survive in their habitat [10,20].

Traditional thin film AR coatings are used in a variety of optical systems and rely on interference. When a single layer dielectric thin film has been deposited on a substrate, the two different interfaces create two reflections, as seen in (a) in the figure below. The AR properties are then obtained when destructive interference forms due to their phase difference, but to achieve minimal reflection, several factors must be optimized: thickness of the thin film, polarization, angle of incidence, and wavelength-dependent reflective index of the film [20]. These highly specific characteristics make it so that only single layer AR coatings are typically possible at a specific wavelength. The AR properties found in the sub-wavelength nano-structure arrays are based on multiple internal reflection and graded changes in refractive index of the substrate [20]. Two different methods of nano-structure formation create AR properties. First, when the unit scale of the structures is larger than the wavelength, it allows the incident light to recognize the individual structures and can partially absorb, reflect or scatter from the individual structures [20]. If the depth scale and spacing of the individual structures are of similar scale to the wavelength of incident light, the light can undergo multiple internal reflections getting trapped between the structures, as shown in (b) of the figure below [20]. Second, if the unit scale of the structures is less than the incident wavelength, the light is insensitive to individual structures and will bend progressively due to graded refractive index changes, demonstrated in (c) of the figure below [20].

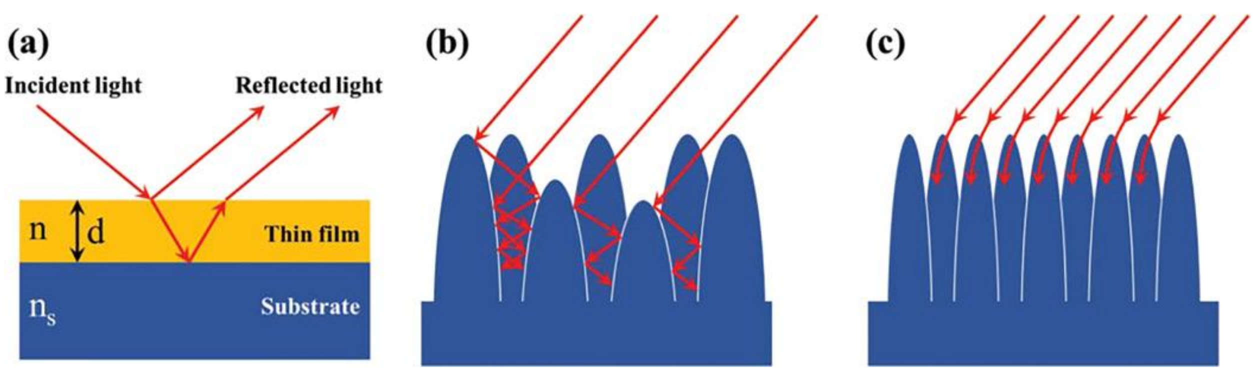

Figure 29. Depictions of incident light propagation through (a) single layer thin-film (n_s>n), (b) micro-scale array of structures, (c) nano-scale array of structures [20].

For x-ray optics, the working scale of surface quality is on the nanoscale, requiring technologies to be able to work on the nanoscale. To work on the nanoscale, current state-of-the-art technologies employed for AR surface production require either time-consuming procedures, complex multistep processes, or chemical processes [10]. The chemical coatings applied to surfaces to create AR coatings degrade in quality over time [10] and may lead to extraneous costs. Laser fabrication of nanostructures on the surface is a maskless process that allows material modification with extreme precision of size and shape of the induced structures.

With traditional thin film deposition, one problem that presents itself is potential stress changes in the mirror substrate due to relaxation or rapid temperature changes. Based on the results of the nanopillar structures produced on fused silica and that ULE performs similarly to fused silica in regards to induced stress state [8], creating these nanopillars on ULE would be beneficial to developing a chemical free way of applying an AR coating for x-ray optics.

3.2 Parametric study

The parameter study was based on the work of Antonis Papadopoulos in reproducing laser induced periodic surface structures (LIPSS) on fused silica [10]. A similar laser system to the one reported in the literature was used to replicate the experiment. The laser parameters reported in Papadopoulos' experiment were slightly different than the parameters needed to operate the laser system available, so the calculations below were performed to find a baseline of parameters to use. The reported parameters reference fluence in energy/area, pulse energy (E_p), laser spot spacing (d), and the effective number of laser scans in an area ($N_{eff,\ 2D}$) [10,21]. The required laser parameter to replicate the experiment included finding appropriate pulse energy, laser repetition rate, laser pulse spacing, line spacing, and writing velocity. In equations 3 – 5, r is the radius of the laser spot, f is repetition rate, ν is the scan speed, and Δ is the line spacing.

$$Fl = 2 \cdot \frac{E_p}{\pi r^2} \tag{3}$$

$$N_{eff,line} = \frac{\pi \cdot r^2 \cdot f}{\nu \cdot \Delta} \tag{4}$$

$$d = 2 \cdot \frac{\nu}{f} \tag{5}$$

Given these equations and the range of working parameters provided by Papadopoulos' experiment, these equations were reworked to find appropriate pulse energies, scan speed that may form nanopillars.

There was uncertainty with how to create the nanopillars with confidence, so a 0.5-mm thick 1-inch fused silica sample was used to perform several parameter scans. The first parameter scan was for finding the ablation threshold by sweeping through 100 steps of pulse energies from 1 μJ to 2 μJ which corresponded to a fluence range of 4.08 to 8.12 $\frac{J}{cm^2}$ respectively. The fluence range that provided uniform nanopillars was between 6 and 7.5 $\frac{J}{cm^2}$. So, by sweeping through this range controlled by pulse energy, the appropriate pulse energies to form nanopillars were narrowed. The 100 squares were 100 μm x 100 μm separated by 100 μm and was only written once. Thorough laser parameters used for the laser written squares were f = 25 kHz, Δ = 10 μm, d = 2.45 μm, τ_p = 350 fs (pulse duration), using a 0.13 NA microscope objective (LMH-5X-1064, Thorlabs) and circular polarization (which was found to be more effective than linear polarization) [10]. These laser parameters were used to closely match the parameters used in the literature [21]. Below is a depiction of this first parameter scan.

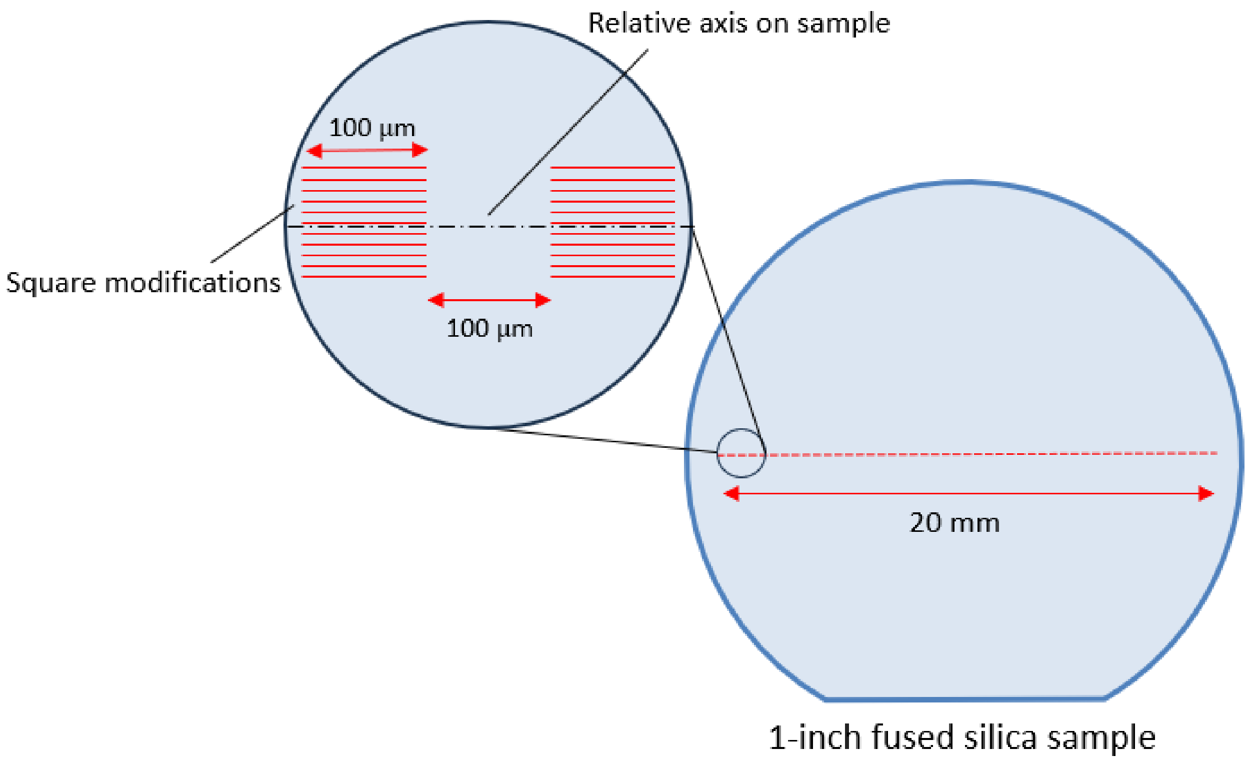

*Figure 30. The first parameter scan performed on fused silica. Pulse energy was stepped from 1 µJ to 2 µJ from right to left in 0.01 µJ steps spanning 20 mm in the center of the sample. *Not to scale.*

The observed laser modified regions (squares) were viewed using an Olympus BX51 Microscope with a DIC prism and multiple objective magnifications. Ablation was clearly visible in different squares when the lines displayed a bright reflection on the lines written. The ablation threshold where the highest pulse energy was used that no ablation occurred was at 1.5 µJ, corresponding to a fluence of 6.12 $\frac{J}{cm^2}$. The microscope image taken using the 40x objective is shown below.

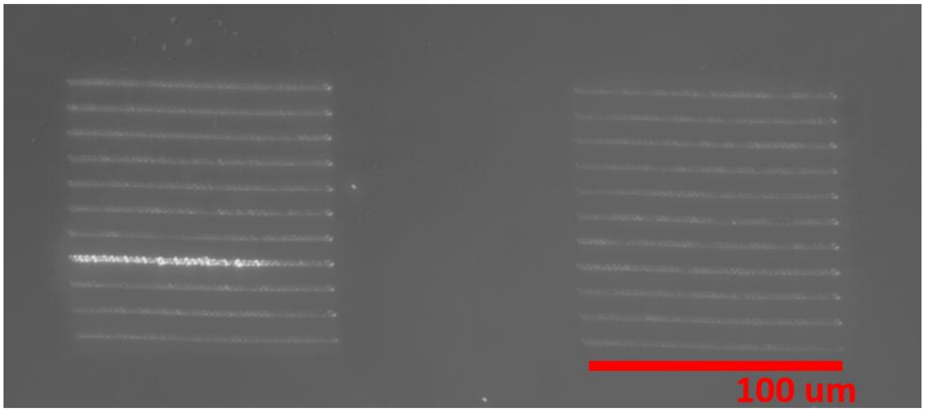

Figure 31. 40x DIC microscope images of ablation threshold found from first parameter scan. Left: E_p *= 1.51 μJ, (fluence = 6.16* $\frac{J}{cm^2}$*) ablation seen in the 4th line from the bottom. Right:* E_p *= 1.5 μJ, (fluence = 6.12* $\frac{J}{cm^2}$*) ablation free lines.*

With the ablation limit found for one scan, the next parameter scan was focused on finding the appropriate combination of pulse energy and number of scans (multiple laser writes in the same area) for nanopillar formation. The second parameter scan used similar laser parameters: f = 25 kHz, d = 2.54 μm, but Δ changed to 5 μm to create a more opaque modification field. A grid-like modification field of the same 100 μm squares in a 6 x 7 array was designed to vary pulse energy in each column (moving right to left) while simultaneously increasing the number of scans in each row (moving downward). The pulse energy ranged from 1.2 μJ to 1.4 μJ and the number of scans ranged from 1 to 7. A depiction is shown below of grid scan 1.

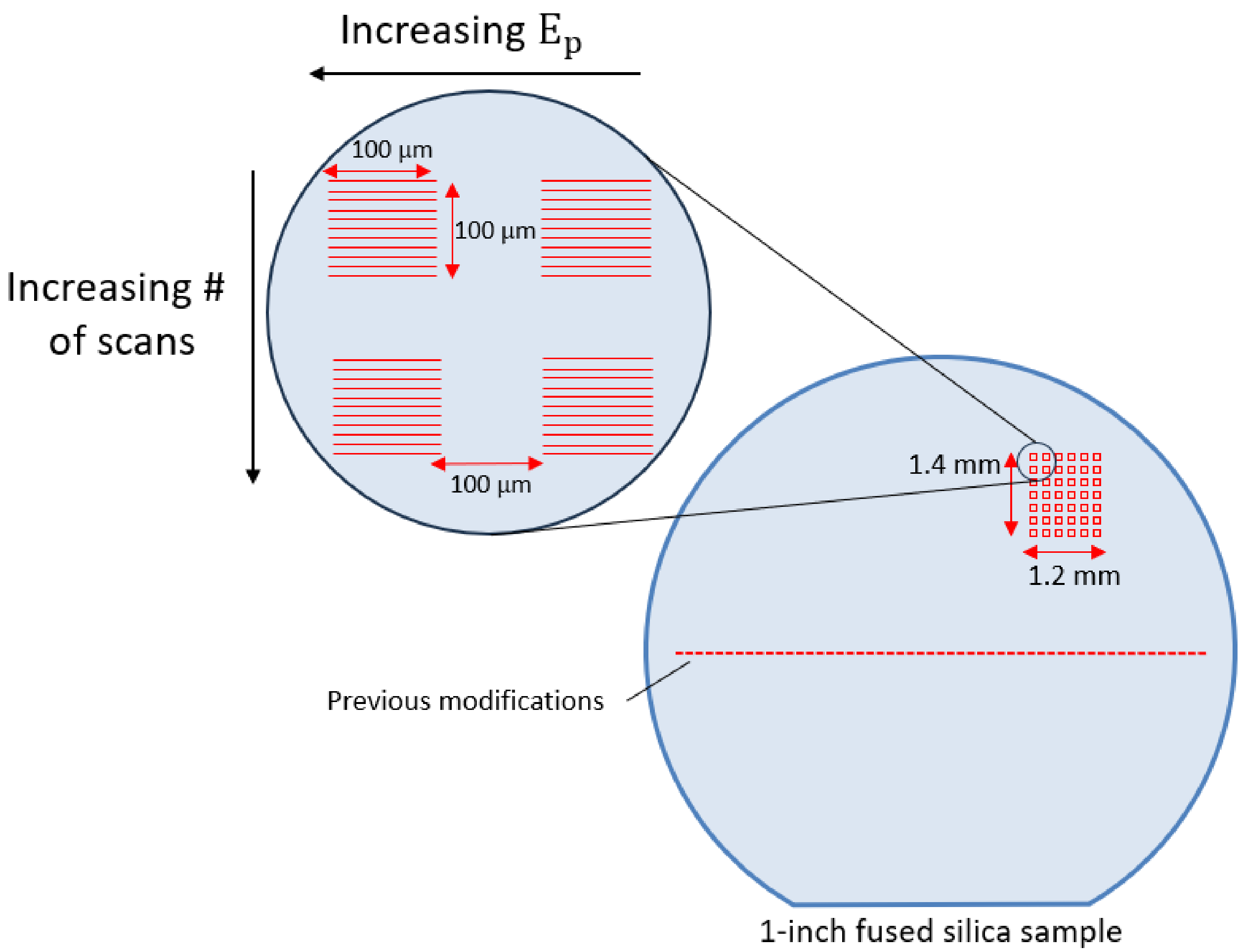

*Figure 32. Depiction of first parameter grid scan on fused silica sample with varying E_p from 1.2 µJ to 1.4 µJ, and varying scan range from 1 to 7 scans. *Not to scale.*

The microscope was used to observe the laser modification squares. The previous ablation threshold scan did not consider multiple scans, so many of the squares resulting from the grid scan parameters were ablated except for some lower pulse energy squares shown below.

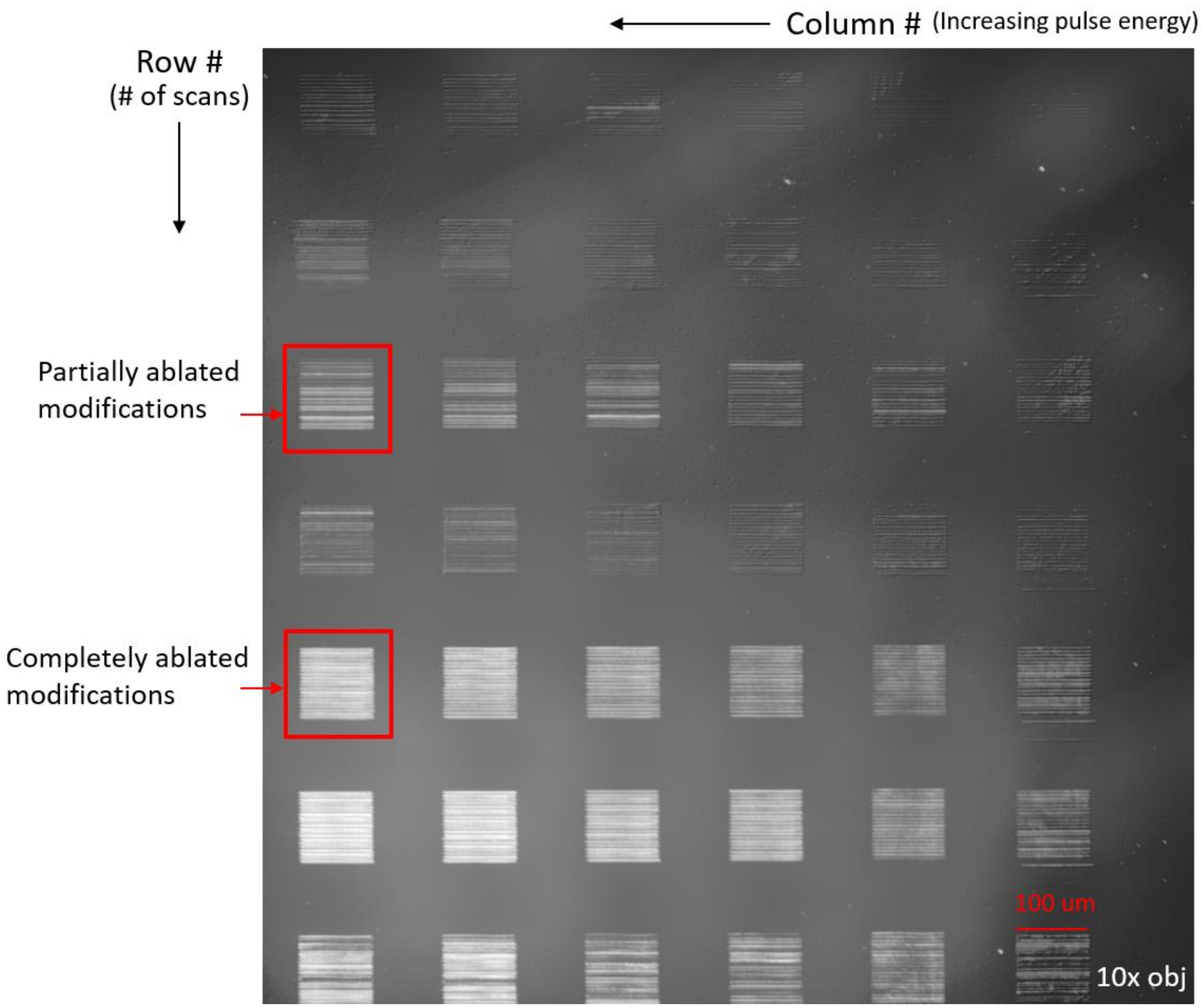

Figure 33. 10x DIC microscope image of grid scan 1. Column corresponding to E_p from right to left [μJ]: 1.19, 1.23, 1.26, 1.33, 1.37.

Given that ablation of the surface happened as early as row 1 column 4, the grid scan was repeated for a lower pulse energy range: 1 μJ to 1.2 μJ. The same parameters and scan range were used for the grid scan 2, see microscope image below. Surface artifacts seen on the right side of the image interacted with the laser and created ablation spots, these were not ablated in response to chosen laser parameters.

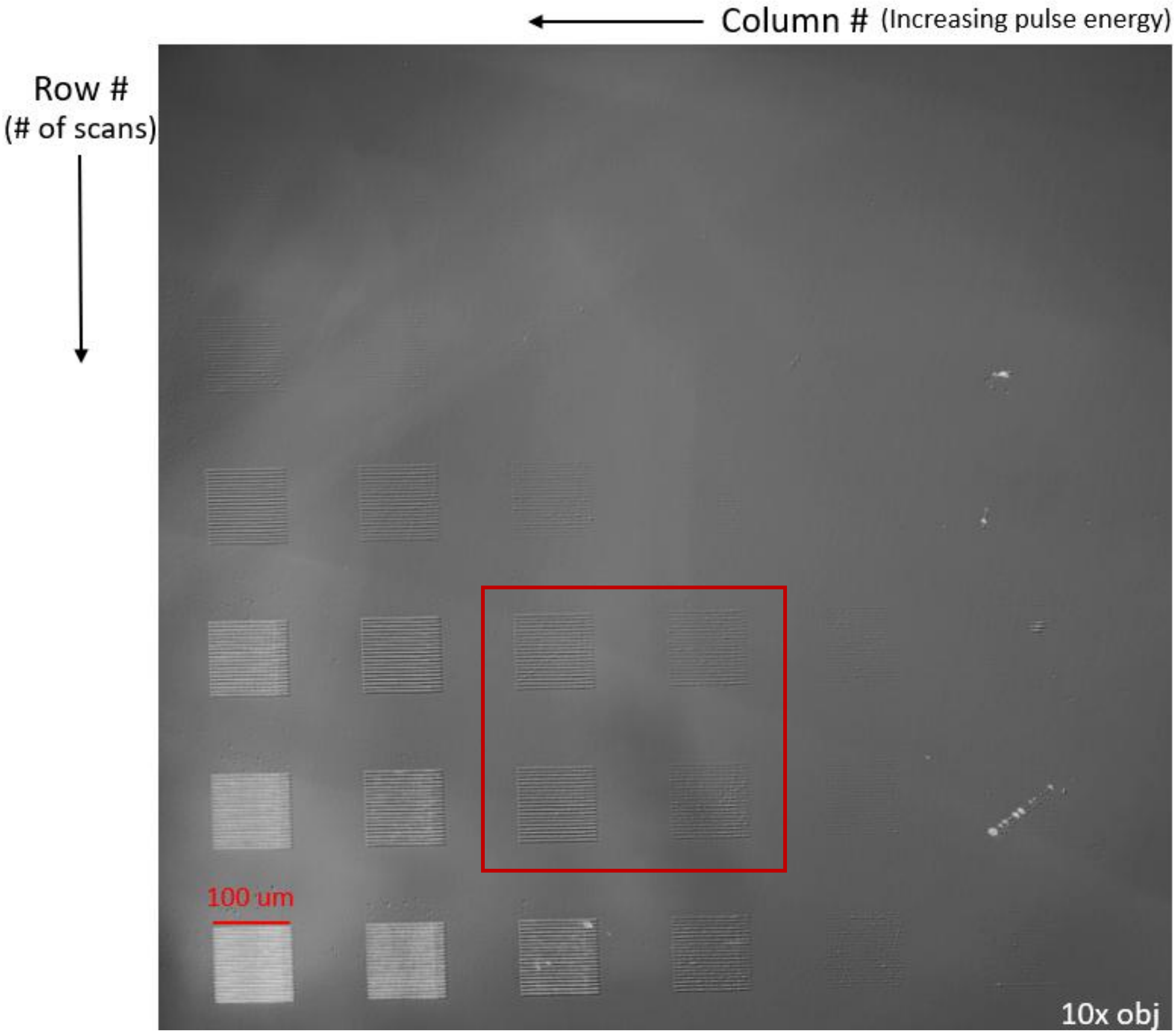

Figure 34. 10x DIC microscope image of grid scan 2. Column corresponding to E_p from right to left [μJ]: 1.0, 1.04, 1.08, 1.12, 1.2. The red square indicates a region of interest for the following parameter test.

The 6 x 7 grid of grid scan 2 narrowed down the laser parameters that might indicate nanopillar formation. How the nanopillars were observed are discussed in section 3.3.

Laser parameters were adjusted to create a larger modified region, from 100 µm x 100 µm squares to 200 µm x 5 mm rectangles. The spot spacing was then decreased from d = 2.54 µm to d = 1.25 µm, and the line spacing was decreased from Δ = 5 µm to Δ = 4 µm. By overlapping the laser spots in a written line around 85%, nanopillars will form more uniformly [10,21]. It was also recommended that when performing line scans, low pulse energy and multiple scans would be more likely to generate nanopillars [21]. As this experiment was a parametric study, small adjustments were made to the parameters iteratively.

Six rectangular modification shapes were written on an unmodified region of fused silica in column separated by 200 μm vertically. The first five rows used a E_p of 1.129 μJ and the row position corresponded to the number of scans. Row six used a E_p of 1.144 μJ at 4 scans to observe any differences that might have arised from pulse energy changes. A microscope image of rows 4, 5, and 6 are displayed in Figure 35. Rows 1 – 3 were not of interest as the modifications were not as visible.

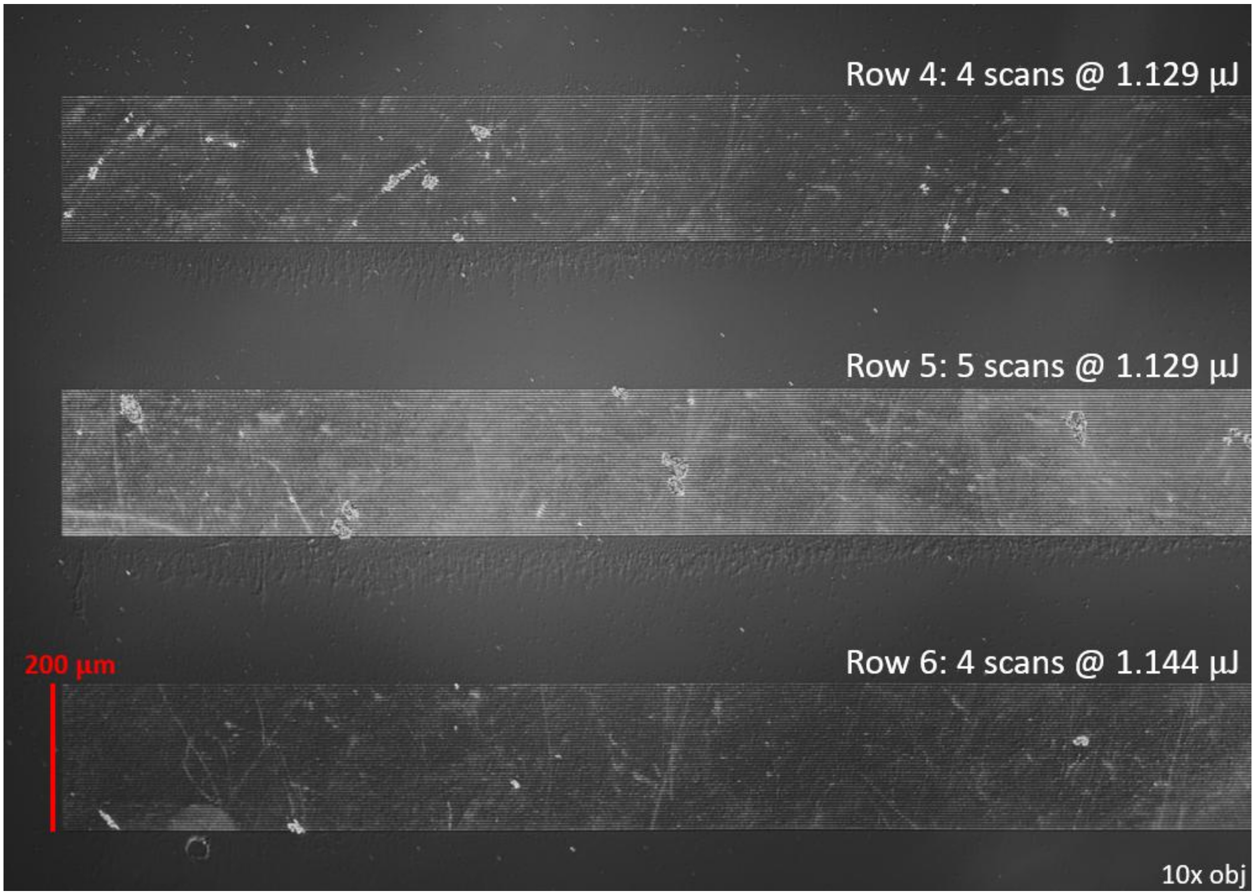

Figure 35. 10x DIC microscope image of rows 4 – 6 of the rectangular modifications on fused silica.

Debris on the surface, sub-surface damage, and surface figure error may affect how the laser modified regions appear after laser writing. The debris will negatively interact with the laser and cause craters to form in the modified regions. However, the debris-free areas of the rectangular regions appeared well defined and ablation-free. The next test scan increased the modified area to 2 mm x 2 mm so that the surface area could be increased for transmission testing with a HeNe laser source. Two of these squares were created using the same laser parameters as row 6 of the rectangular modification but at 2 and 3 scans respectively.

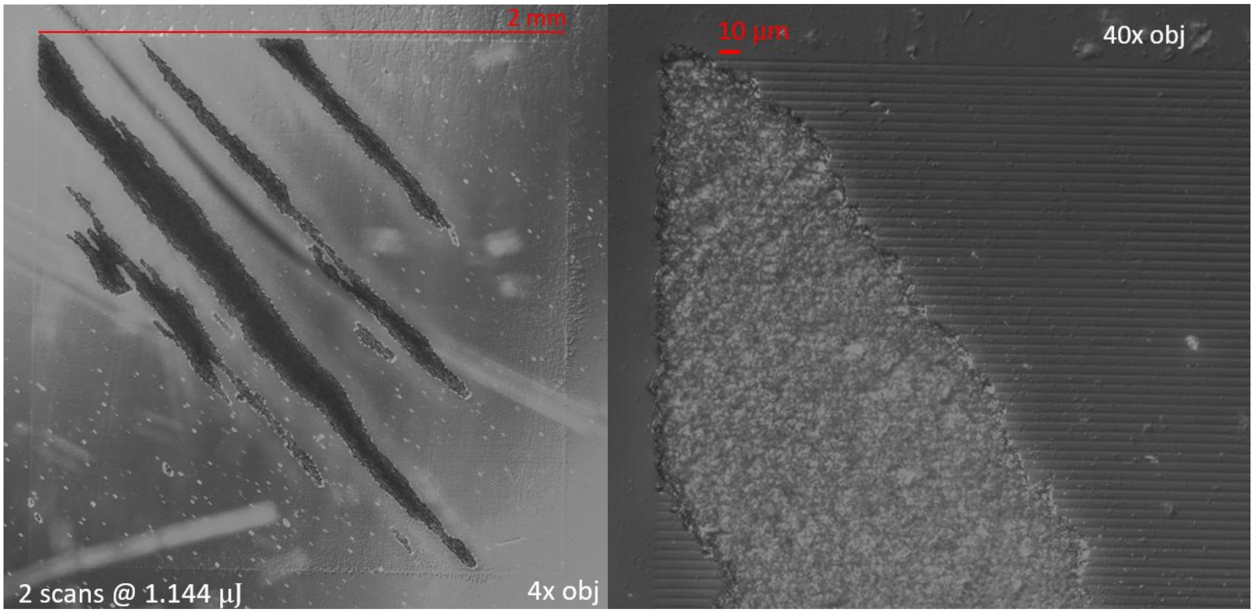

Figure 36. Microscope DIC images of 2 mm square modification. Left: 4x objective showing surface figure error. Right: 40x objective of top left region showing surface figure error created ablation.

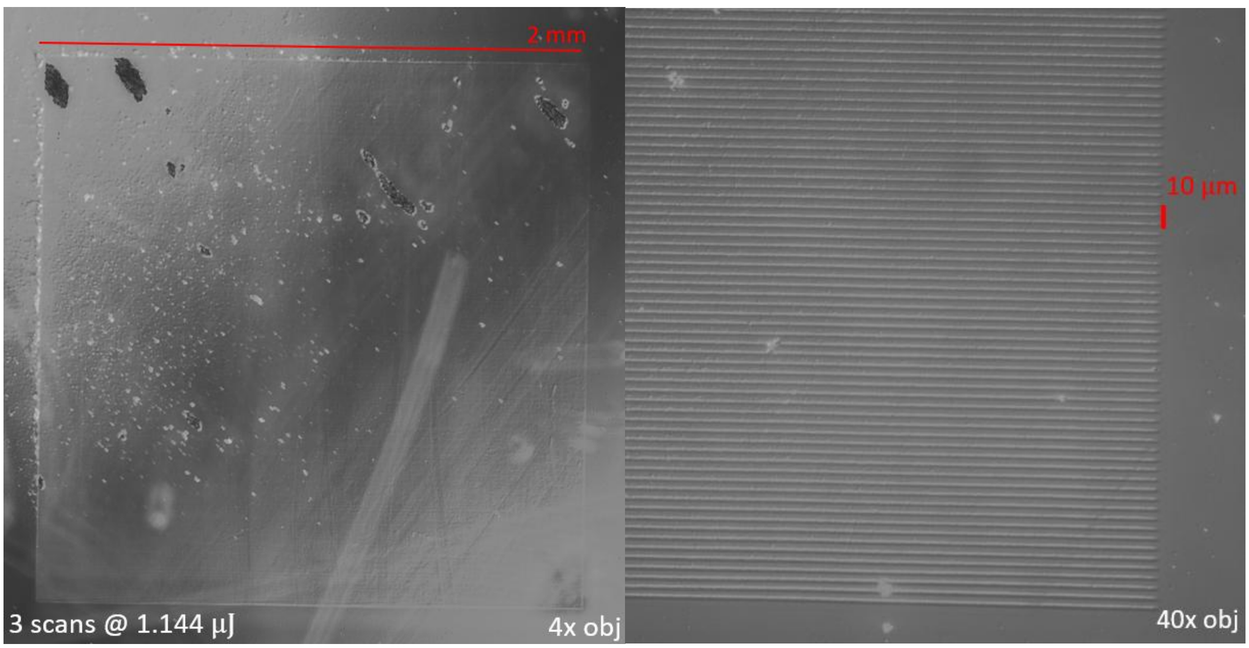

Figure 37. Microscope DIC images of second 2 mm square. Left: 4x objective showing slight surface figure error. Right: 40x objective of bottom right region with little to no surface defects.

Once the 2 mm squares were imaged, the laser parameters used were found sufficient to move on to ULE.

Although ULE has similar properties and characteristics to fused silica, ULE has a lower melting point than fused silica, so the pulse energy had to be reduced to avoid surface ablation. The first parametric scan on ULE was performed using f = 25 kHz, Δ = 3 µm, d = 1.25 µm, and E_p = 1.038 µJ to create 200 µm by 5 mm rectangles on a 1-inch ULE wafer. Four rows of these rectangular modifications were created where the row corresponded to number of scans. The last two rows, 3 and 4 scans, showed that surface figure error likely printed through in the third row, and ablation occurred in the fourth row, shown below.

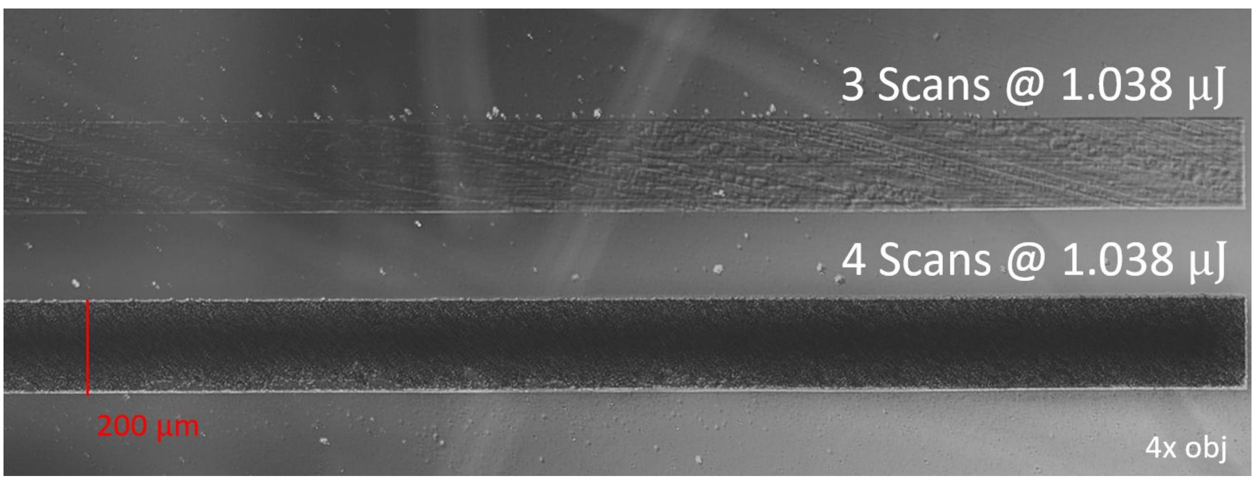

Figure 38. 4x microscope DIC image of the right side of row 3 & 4 of the first ULE parameter scan.

Due to the ablated region of row 4, the next parameter scan repeated the first scan with the same parameters, but at E_p = 1.0 µJ so that the scan range could be increased without reaching ablation. The second parameter scan on ULE featured four rectangular rows of 2 mm length instead of 5 mm length so all modified regions could be seen under the microscope. The measurement of the nanopillars formed in the modified region of row 3 (3 scans) below ended up resulting in the final parameters deemed for nanopillar creation on ULE. The large triangular ablated area in row 3 is likely to be surface figure error that negatively interacts with the laser writing.

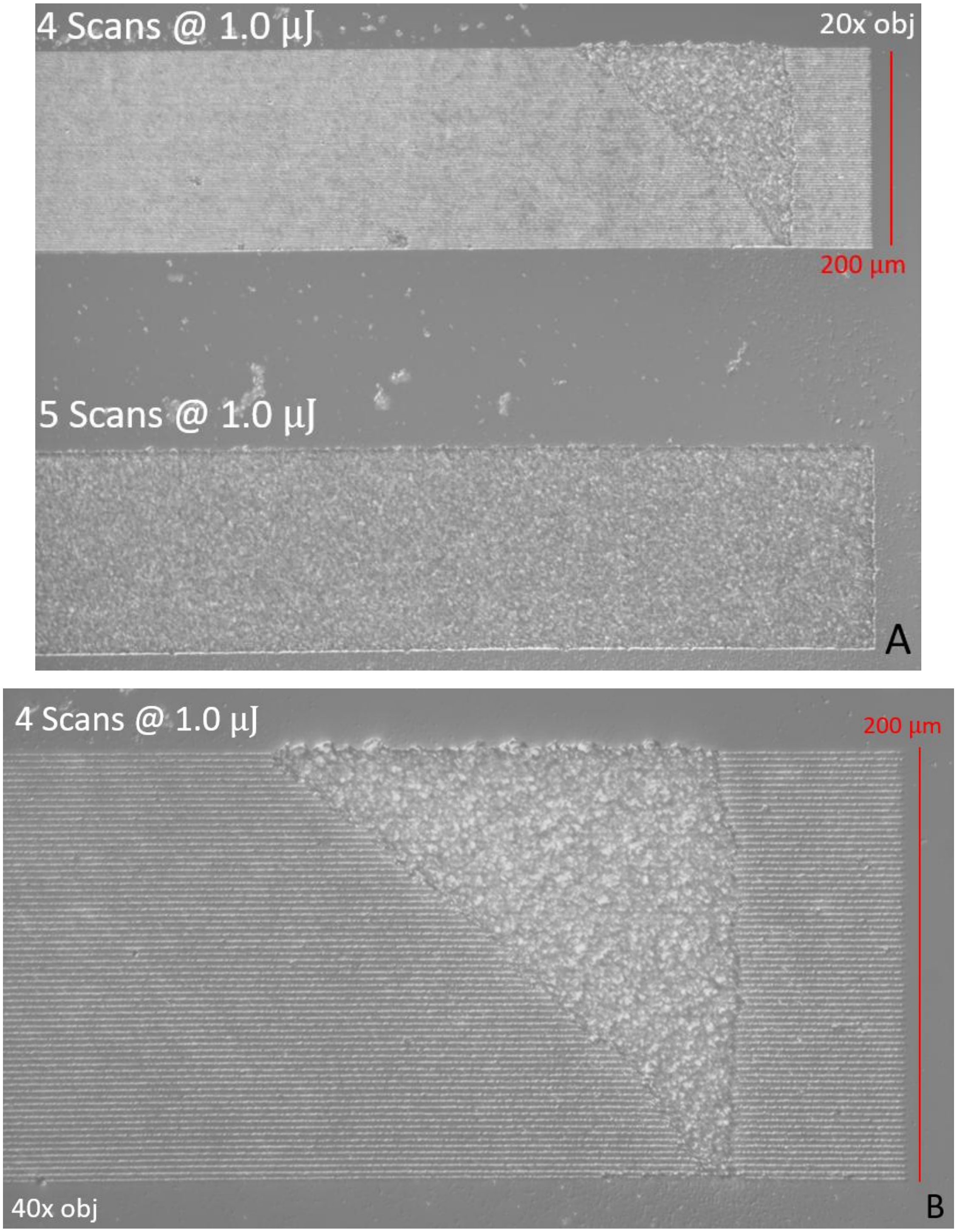

Figure 39. DIC microscope images of the right side of the second parameter scan on ULE. A) 20x objective showing rows 3 & 4. B) 40x objective showing row 3.

3.3 Surface structure characterization

The nanopillars formed in each iteration of a parameter scan were roughly 100 to 200 nm tall and between 50 to 200 nm apart, unable to be detected with the largest magnification available from the microscope, a 0.65 NA. The diffraction limited resolution of the microscope used was about 0.52 µm [22]. Traditionally, a scanning electron microscope (SEM) would be utilized to measure the surface structure at such a small scale, but through the coating process, the surface would inherently be damaged. The atomic force microscope (AFM) has the capability to measure at such a small scale while not damaging the laser modified region.

Four square modification regions of grid scan 2 on the fused silica sample were measured using the AFM. The AFM measuring parameters were similar to the parameters used in measuring the surface roughness of samples in the previous chapter. A 1 µm x 1 µm field was measured in each square at 0.5 Hz, a slower rate due to the surface being much rougher. Gwyddion was used in a similar fashion to quantify the height of nanopillars formed. Below are the AFM images of the fused silica squares that seemed likely to form nanopillars.

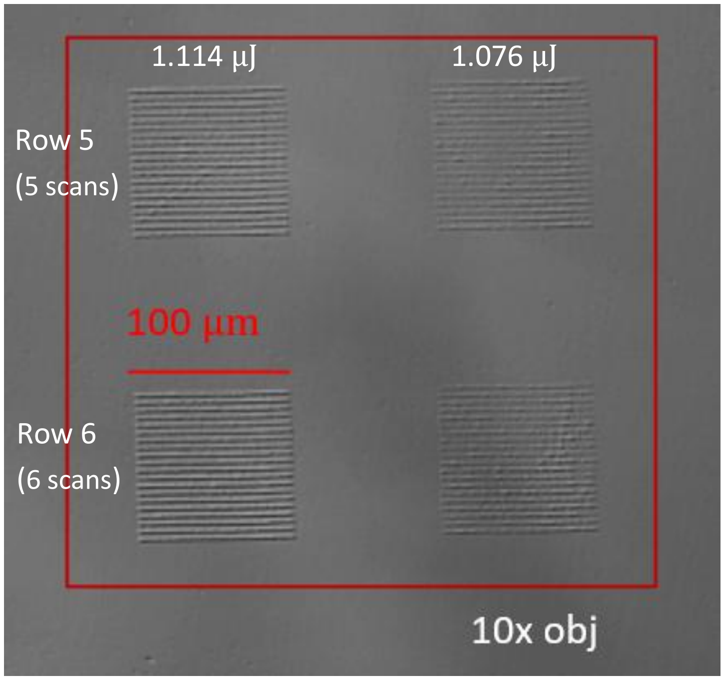

Figure 40. 10x microscope DIC image of fused silica grid scan 2. (rows 5-6, columns 3-4).

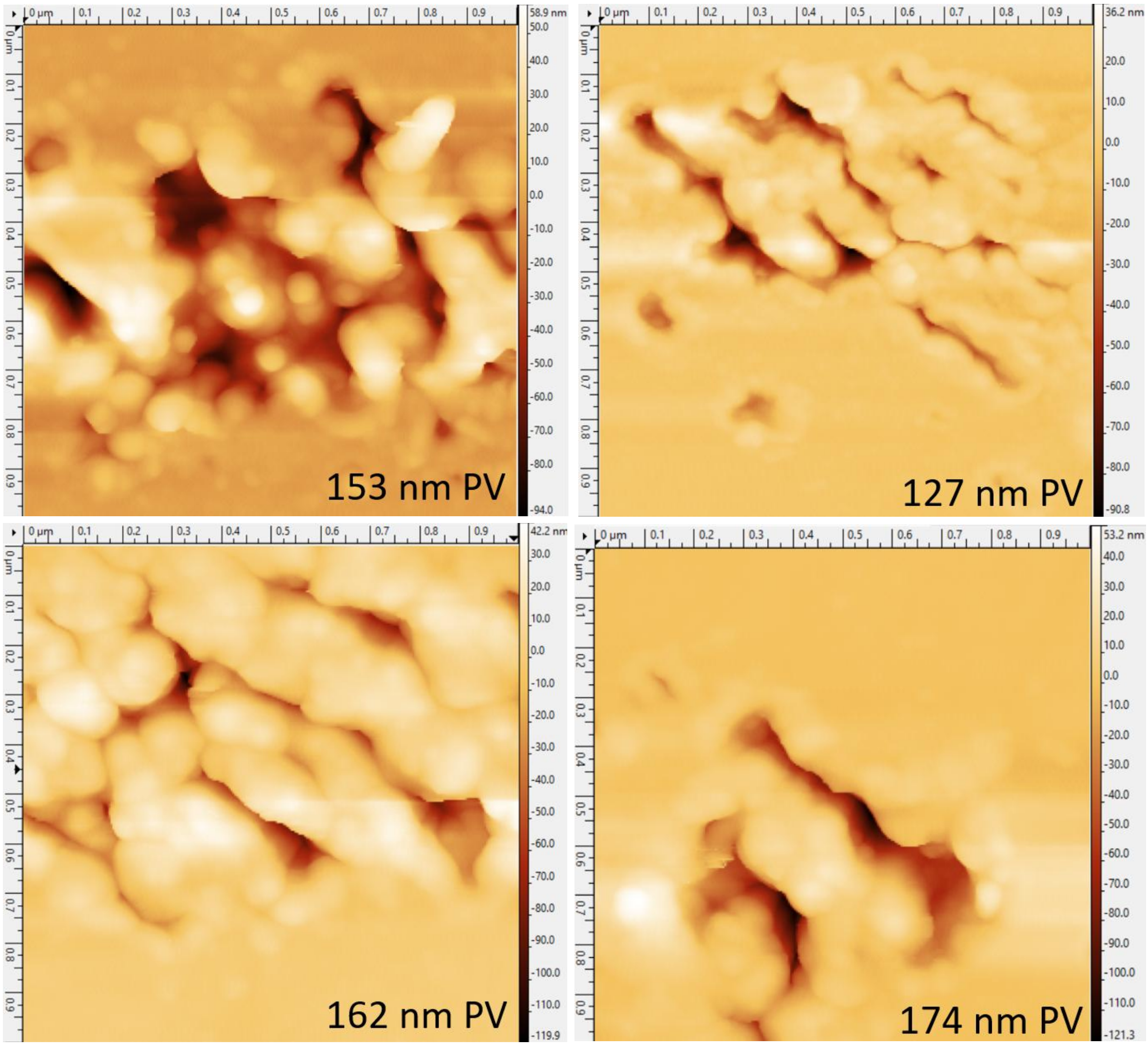

Figure 41. 1 µm x 1 µm AFM images corresponding to the square modifications of interest on fused silica grid scan 2 (see previous figure for correlation). The peak-to-valley heights are noted on each image.

With the peak-to-valley heights of the nanopillars between 100 – 200 nm, this agreed with the heights of the nanopillars observed in the experiments from Papadopoulos using an SEM [10].

The third row of the second parameter scan on ULE was measured with the AFM in two different locations of the rectangle.

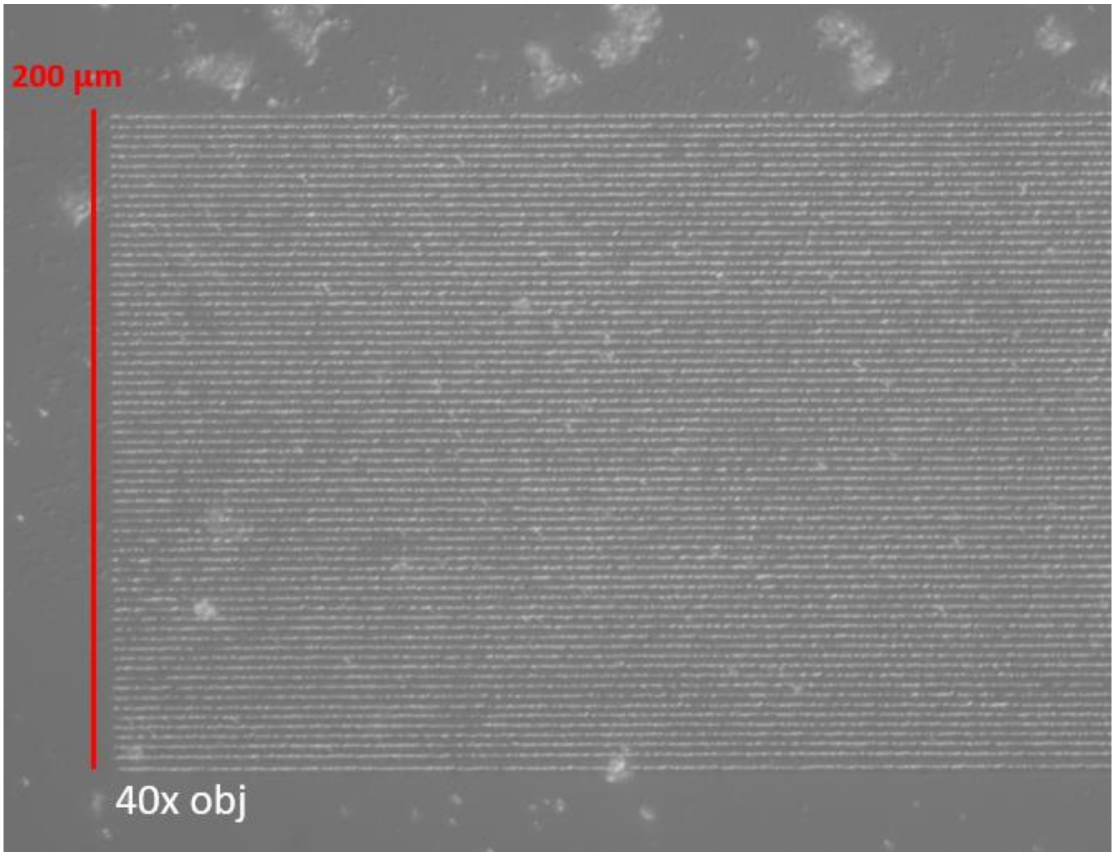

Figure 42. 40x microscope DIC image of the left side of row 3 of the second parameter scan on ULE. This was 4 scans at E_p = 1 μJ.

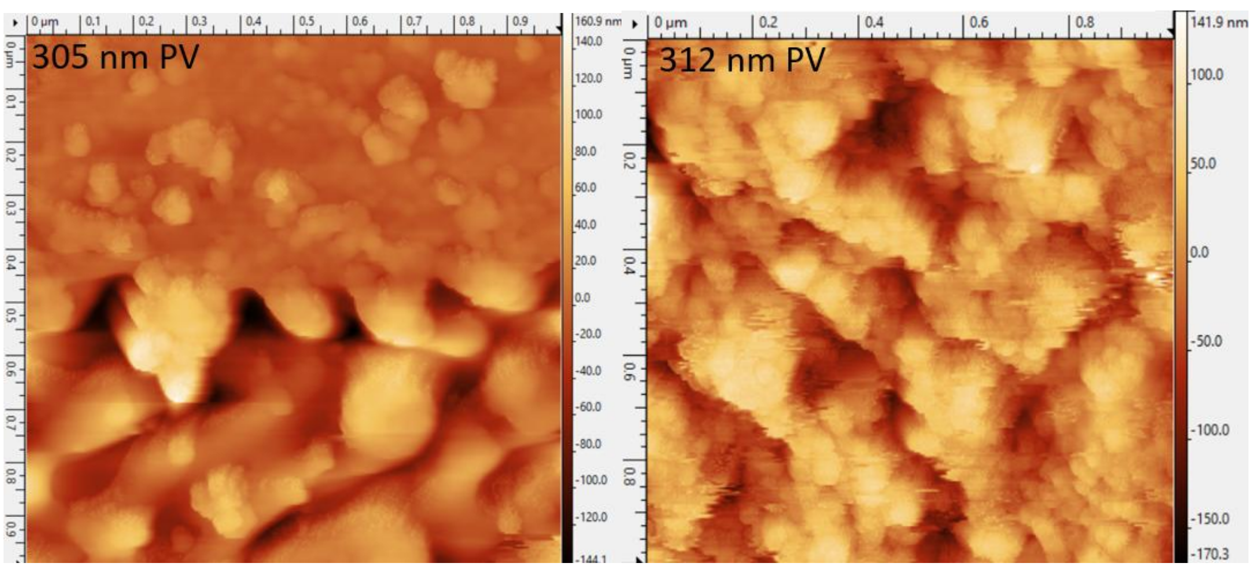

Figure 43. Two 1 µm x 1 µm AFM fields measured on row 3 of the second ULE parameter scan. Left: measured in the middle of the sample. Right: measured on the right side of the sample. Laser parameters:4 scans at E_p = 1 μJ, f = 25 kHz, Δ = 3 µm, d = 1.25 µm, τ_p = 350 fs.

The AFM image on the right above looked representative of nanopillars, and at the scale of 300 nm with no ablation, the surface roughness is more than sufficient to act as an AR coating for x-rays.

To further quantify the results of the nanopillars, a HeNe source on an Apre S100 Fizeau interferometer, with the transmission reference flat removed, was used to observe the reflectance effects from the nanopillar structures. This allowed the only optical cavity present to be the physical thickness of the sample. Both the fused silica wafer and ULE wafer were placed on a hexapod mount in the view of the HeNe source. In the interferometric image shown below, the concentric rings observed are due to the optical path difference (OPD) between the two surfaces of the 0.5 mm thick fused silica wafer [23]. The fringes are useful in observing the reflectance from the unmodified region of the wafer to the modified regions. From the last parameter scan on fused silica creating the 2 mm square, it is seen that the square region is less bright than the region outside of the square, indicating lower reflectance of the source light. This means that the nanopillars created are behaving as expected, reducing the reflectance from visible light. Also agreeing with what was found in Papadopoulos' experiment regarding reflectance reduction [10].

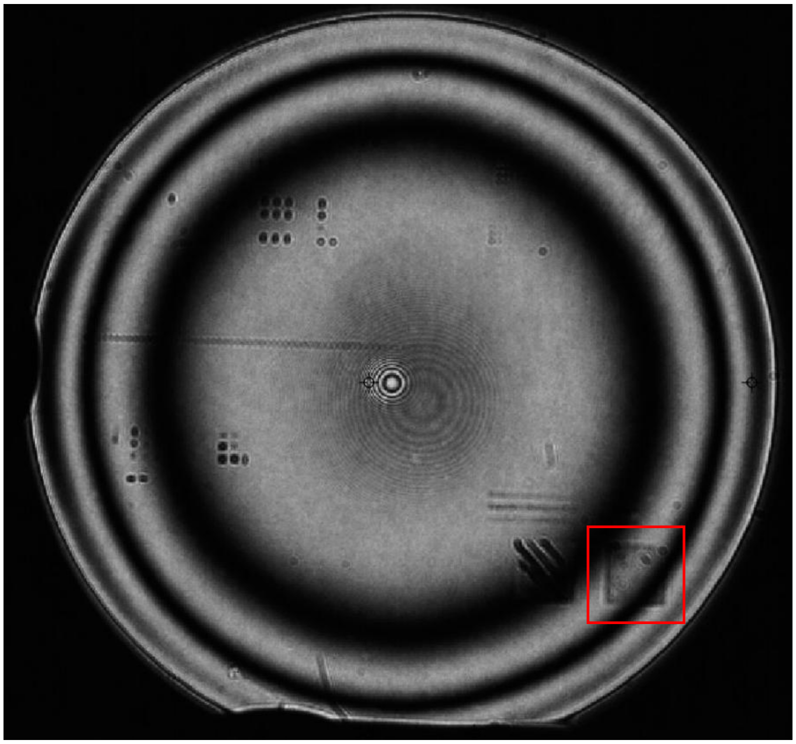

Figure 44. Interferometric image of the 1-inch fused silica wafer using a HeNe source. The highlighted red square is the second 2 mm square demonstrating lower reflectance.

Similarly, the 1-inch ULE wafer with the laser modifications was placed in the mount in front of the HeNe source. The ULE wafer was 1 mm thick and appeared to have a larger thickness variation as the interference rings were not completely concentric nor centered. In the figures below, the 3rd row of the second scan of 2 mm x 200 μm rectangular modifications was the region that measured in the 300 nm range of nanopillar height. It is difficult to see on the interferometer, however on the edges of the dark ring crossing through the rectangular region, the modified region appears darker than the unmodified region. This suggests that the nanopillars formed on ULE are creating a reduction in reflection.

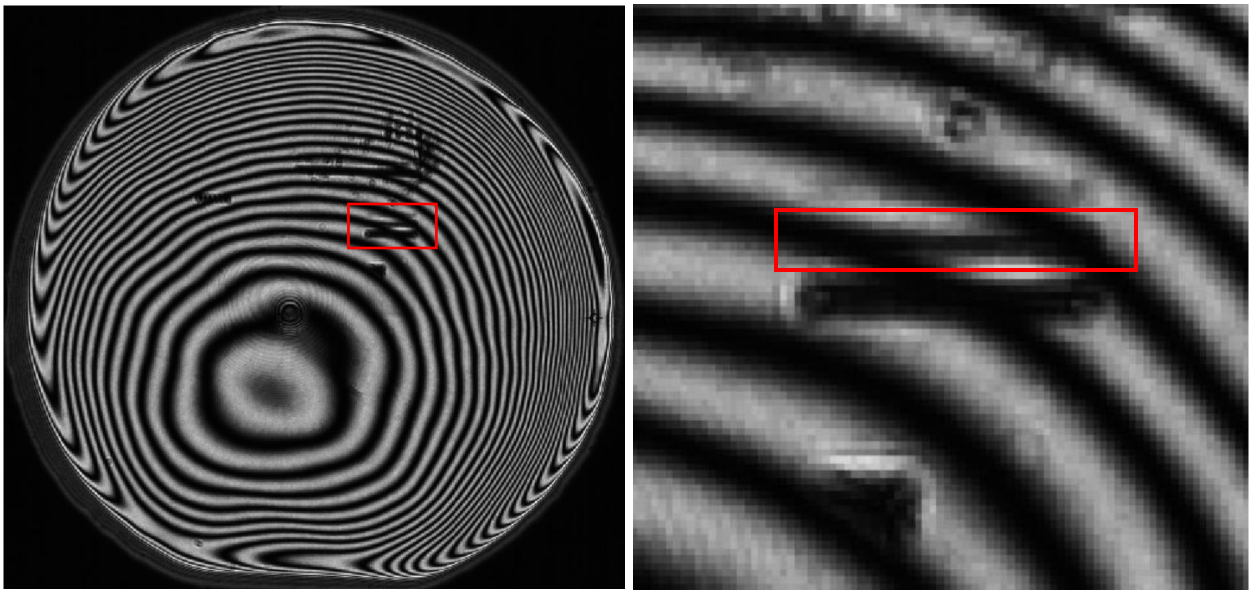

Figure 45. Interferometric images of the 1-inch ULE wafer with a HeNe source. Left: Full wafer image with red rectangle highlighting the second parameter scan of 2 mm long rectangular modifications. Right: The third row of the rectangular modifications highlighted by the red outline.

3.4 Discussion

Creating the nanopillar modifications on fused silica prior to creating them on ULE was to ensure that the parameter scans used in this experiment were producing similar results to those found in literature. Replication of the nanopillars structure has been done on fused silica, zinc sulfide, and sapphire materials [24,25], but not ULE yet. From this experiment, the creation of the nanopillar structures on ULE indicate that laser-induced modifications may be a viable option to create AR coatings for space-based optical systems, especially those relating to x-ray optics.

The nanopillars created on the 1-inch wafers were at a small scale, so scaling up to commercial production would likely require changes to the laser writing system. Incorporating a microlens array (MLA) would allow the sample to be modified faster as it would create an array of many laser spots focusing on the substrate instead of 1 for example, as seen in the work of

Zhang, et al [24]. By incorporating an MLA, the depth and period of the nanopillars could be easily adjusted by the laser scanning speed and distance between the objective lens and the MLA [24]. A similar component to the MLA would be a diffractive optical element (DOE) which would also allow multiple laser spots to be written simultaneously. Another commercial scale improvement to the laser writing system would be to use a Galvo system instead of motorized linear stages that are used for the current laser system. A Galvo system would also speed up the processing time [26].

Further investigation of the nanopillars on ULE regarding this experiment should consider measuring the reflectance with a spectrometer to further quantify the effects of the laser modified region. Laser writing a larger area such as a 2 mm square or an entire 1-inch wafer of ULE may provide more information when using measurement devices like the Fizeau interferometer and would provide a clearer result.

Chapter 4 – Conclusion

This work examined two key areas relevant to x-ray mirror fabrication: the impact of chemical etching on surface roughness, and the feasibility of laser-induced nanopillars as anti-reflection (AR) coatings. It was found that chemical etching did not significantly degrade the surface roughness of ULE substrates, indicating that this process is suitable for fabricating complex geometries, like flexures. Laser modifications written on fused silica and ULE glass successfully produced nanopillar structures approximately 300 nm tall using low pulse energies and multiple passes. These nanopillars show potential as a chemical-free AR coating solution for reducing reflectance on the back surface of x-ray mirrors. Further experiments measuring surface roughness from other transparent substrates and reflectance analysis of the nanopillar structure would increase confidence in these results. Overall, this work supported the continued development of laser-based fabrication techniques for future x-ray telescope missions.

References

1. F. E. Christensen and B. D. Ramsey, "X-ray Optics for Astrophysics: A Historical Review," in *Handbook of X-Ray and Gamma-Ray Astrophysics*, C. Bambi and A. Santangelo, eds. (Springer Nature Singapore, 2024), pp. 73–114.
2. C. Atkins, "Technologies for Advanced X-ray Mirror Fabrication," in *Handbook of X-Ray and Gamma-Ray Astrophysics*, C. Bambi and A. Santangelo, eds. (Springer Nature Singapore, 2024), pp. 371–409.
3. W. W. Zhang, K. D. Allgood, M. P. Biskach, K.-W. Chan, M. Hlinka, J. D. Kearney, J. R. Mazzarella, R. S. McClelland, A. Numata, and R. E. Riveros, "High-resolution, lightweight, and low-cost x-ray optics for the Lynx observatory," J. Astron. Telesc. Instrum. Syst. **5**, 1 (2019).
4. B. L. Henke and E. M. Gullikson, "X-ray interactions: photoabsorption, scattering, transmission, and reflection at E=50-30000 eV, Z=1-92," https://henke.lbl.gov/optical_constants/.
5. K. K. Madsen, D. Broadway, and D. D. M. Ferreira, "Single-Layer and Multilayer Coatings for Astronomical X-ray Mirrors," in *Handbook of X-Ray and Gamma-Ray Astrophysics*, C. Bambi and A. Santangelo, eds. (Springer Nature Singapore, 2024), pp. 177–215.
6. B. D. Chalifoux, K. A. Laverty, and I. J. Arnold, "Ultrafast laser stress figuring for accurate deformation of thin mirrors," Opt. Express **30**, 17767 (2022).
7. C. A. Ross, D. G. MacLachlan, D. Choudhury, and R. R. Thomson, "Optimisation of ultrafast laser assisted etching in fused silica," Opt. Express **26**, 24343 (2018).
8. K. A. Laverty, D. Kim, J. B. Johnson, M. Echter, and B. D. Chalifoux, "Investigation of ultrafast laser stress generation in fused silica, Corning Eagle XG glass, Corning ULE glass, and sapphire," in (Proc. of SPIE, 2023), Vol. 12669, p. 1266907.
9. W. W. Zhang, "Manufacture of mirror glass substrates for the NuSTAR mission," in (Proc. of SPIE, 2009), Vol. 7437, p. 74370N.
10. A. Papadopoulos, E. Skoulas, A. Mimidis, G. Perrakis, G. Kenanakis, G. D. Tsibidis, and E. Stratakis, "Biomimetic Omnidirectional Antireflective Glass via Direct Ultrafast Laser Nanostructuring," Advanced Materials **31**, 1901123 (2019).
12. M. Pfiffer, P. Cormont, E. Fargin, B. Bousquet, M. Dussauze, S. Lambert, and J. Néauport, "Effects of deep wet etching in HF/HNO_3 and KOH solutions on the laser damage resistance and surface quality of fused silica optics at 351 nm," Opt. Express **25**, 4607 (2017).
13. F. J. Fuchs, "Ultrasonic cleaning and washing of surfaces," in *Power Ultrasonics* (Elsevier, 2015), pp. 577–609.
14. R. R. L. De Oliveira, D. A. C. Albuquerque, T. G. S. Cruz, F. M. Yamaji, and F. L. Leite, "Measurement of the Nanoscale Roughness by Atomic Force Microscopy: Basic Principles and Applications," in *Atomic Force Microscopy - Imaging, Measuring and Manipulating Surfaces at the Atomic Scale*, V. Bellitto, ed. (InTech, 2012).
15. D. Nečas and P. Klapetek, "Gwyddion: an open-source software for SPM data analysis," Open Physics **10**, 181–188 (2012).
16. J. C. Wyant, "White Light Interferometry," Proc. of SPIE **4737**, 98–107 (2002).
17. Zygo, "NewView 9000 Specifications," (2025).
18. S. M. Iles and J. J. Nelson, "Sub-angstrom surface roughness metrology with the white light interferometer," in (Proc. of SPIE, 2019), Vol. 11175, p. 117519.
19. T. I. Suratwala, *Materials Science and Technology of Optical Fabrication*, 1st ed. (Wiley, 2018).
20. H.-J. Choi, D. Huh, J. Jun, and H. Lee, "A review on the fabrication and applications of sub-wavelength anti-reflective surfaces based on biomimetics," Applied Spectroscopy Reviews **54**, 719–735 (2019).

21. A. Papadopoulos, E. Skoulas, A. Mimidis, G. Perrakis, G. Kenanakis, G. D. Tsibidis, and E. Stratakis, "Supporting Information: Biomimetic Omnidirectional Antireflective Glass via Direct Ultrafast Laser Nanostructuring," Advanced Materials **31**, 1901123 (2019).
22. "Olympus System Microscope BX51 Instructions," (2007).
23. F. A. Jenkins and H. E. White, *Fundamentals of Optics CH 14*, 4th ed. (Mc Graw-Hill Primis Custom Publ, 2001).
24. F. Zhang, J. Duan, X. Zhou, and C. Wang, "Broadband and wide-angle antireflective subwavelength microstructures on zinc sulfide fabricated by femtosecond laser parallel multi-beam," Opt. Express **26**, 34016 (2018).
25. H. K. Raut, V. A. Ganesh, A. S. Nair, and S. Ramakrishna, "Anti-reflective coatings: A critical, in-depth review," Energy Environ. Sci. **4**, 3779 (2011).
26. G. Meng, L. Jiang, X. Li, Y. Xu, X. Shi, R. Yan, and Y. Lu, "Dual-scale nanoripple/nanoparticle-covered microspikes on silicon by femtosecond double pulse train irradiation in water," Applied Surface Science **410**, 22–28 (2017).
27. M. J. Pivovaroff and T. Okajima, "Geometries for Grazing Incidence Mirrors," in *Handbook of X-Ray and Gamma-Ray Astrophysics*, C. Bambi and A. Santangelo, eds. (Springer Nature Singapore, 2024), pp. 115–135.